

**THE SECOND GENERATION CURVELET TRANSFORM IN THE
ANALYSIS OF 2-D GPR DATA: SIGNAL ENHANCEMENT AND
RETRIEVAL OF ORIENTATION-AND-SCALE-DEPENDENT
INFORMATION**

Andreas Tzanis

*Department of Geophysics and Geothermy,
National and Kapodistrian University of Athens,
Panepistimioupoli,
Zografou 15784, Greece.
E-mail: atzanis@geol.uoa.gr*

Athens, October 2013

LICENSE

Copyright © 2013, Andreas Tzanis.

Dr Andreas Tzanis
Department of Geophysics,
University of Athens
Panepistimioupoli,
Zografou 15784
Greece
Tel: +30-210-727-4785
E-mail: atzanis@geol.uoa.gr

Permission is granted to copy and distribute this document, but not to modify any part of the document under any circumstances and without exception. The context of “copying” and “distributing” the document should be understood in terms of the GNU Free Documentation License, Version 2 or any later version published by the Free Software Foundation.

Abstract

The Ground Probing Radar (GPR) is a valuable tool for near surface geological, geotechnical, engineering, environmental, archaeological and other work. GPR images of the subsurface frequently contain geometric information (constant or variable-dip reflections) from various structures such as bedding, cracks, fractures etc. Such features are frequently the target of the survey; however, they are usually not good reflectors and they are highly localized in time and in space. Their scale is therefore a factor significantly affecting their detectability. At the same time, the GPR method is very sensitive to broadband noise from buried small objects, electromagnetic anthropogenic activity and systemic factors, which frequently blurs the reflections from such targets. The purpose of this paper is to investigate the Curvelet Transform (CT) as a means of S/N enhancement and information retrieval from 2-D GPR sections, with particular emphasis on the recovery of features associated with specific temporal or spatial scales and geometry (orientation/dip).

The CT is a multiscale and multidirectional expansion that formulates an optimally sparse representation of bivariate functions with singularities on twice-differentiable (C^2 -continuous) curves (e.g. edges) and allows for the optimal, whole or partial reconstruction of such objects. The CT can be viewed as a higher dimensional extension of the wavelet transform: whereas discrete wavelets are isotropic and provide sparse representations of functions with point singularities, curvelets are highly anisotropic and provide sparse representations of functions with singularities on curves. A GPR section essentially comprises a spatio-temporal sampling of the transient wavefield which contains different arrivals that correspond to different interactions with wave scatterers in the subsurface (wavefronts). These are generally longitudinally piecewise smooth and transversely oscillatory, i.e. they comprise edges. Curvelets can detect wavefronts at different angles and scales because curvelets of a given angle and scale locally correlate with aligned wavefronts of the same scale.

The utility of the CT in processing noisy GPR data is investigated with software based on the Fast Discrete CT (Candès et al. 2006) and adapted for use with a set of interactive driver functions that compute and display the curvelet decomposition and then allow the manipulation of data (wavefront) components at different scales and angles via the corresponding manipulation (cancelation or restoration) of their associated curvelets. The method is demonstrated with data from archaeometric, geotechnical and hydrogeological surveys, contaminated by high levels of noise, or featuring straight and curved reflections in complex propagation media, or both. It is shown that the CT is very effective in enhancing the S/N ratio by isolating and cancelling directional noise wavefronts of any scale and angle of emergence, sometimes with surgical precision and with particular reference to clutter. It can as successfully be used to retrieve waveforms of specific scale and geometry for further scrutiny, also with surgical precision, as for instance distinguish signals from small and large aperture fractures and faults, different phases of fracturing and faulting, bedding etc. Moreover, it can be useful in investigating the characteristics of signal propagation (hence material properties), albeit indirectly. This is possible because signal attenuation and temporal localization are closely associated, so that scale and spatio-temporal localization are also closely related. Thus, interfaces embedded in low attenuation domains will tend to produce sharp reflections and fine-scale localization. Conversely, interfaces in high attenuation domains will tend to produce dull reflections with broad localization.

1 Introduction

The Ground Probing Radar (GPR) has become a valuable, almost indispensable means of exploring near surface structures for geological, geotechnical, engineering, environmental, archaeological and other work. The purpose of this paper is to investigate methods of S/N enhancement and geometrical information retrieval from GPR data, with particular emphasis placed on the problem of recovering features associated with specific temporal or spatial scales and geometry (orientation/dip).

GPR data essentially comprise recordings of the amplitudes of transient waves generated and detected by source and receiver antennae, with each source/receiver pair generating a data trace that is a function of time. An ensemble of traces collected sequentially along a scan line, i.e. a GPR section or B-scan, provides a spatio-temporal sampling of the wavefield which contains different arrivals that correspond to different interactions with wave scatterers (inhomogeneities) in the subsurface. All these arrivals represent wavefronts that are relatively smooth in their longitudinal direction and oscillatory in their transverse direction. Thus, GPR images frequently contain geometric (orientation/dip-dependent) information from point scatterers (e.g. diffraction hyperbolae), dipping reflectors (geological bedding, structural interfaces, cracks, fractures and joints), as well as other conceivable structural configurations. In geological, geotechnical and engineering applications, one of the most significant objectives is the detection of fractures, inclined interfaces and empty or filled cavities frequently associated with jointing/faulting; these types of target, especially fractures, are usually not good reflectors and are spatially localized.

At the same time, GPR data is notoriously susceptible to noise. For example, boulders, animal burrows, trees, tree roots, and other small scale objects and structures can cause unwanted reflections or scattering. Anthropogenic noise is worse and can include reflections from nearby vehicles, buildings, fences and power lines. Transmissions from cellular telephones, two-way radios, television, and radio and microwave devices may also cause noise. These types of reflections are only partially countered with shielded antennae while the interference by extraneous or reflected airwaves, critically refracted airwaves and groundwaves cannot be easily suppressed during acquisition. Finally, there's systemic noise, frequently manifested in the form of ringing (antenna self-clutter). In many cases, the noise has definite directional characteristics (e.g. high-angle crossing clutter). Because the GPR source wavelet is tuned at a single operating frequency, the information returned by the subsurface structure is usually limited to a relatively narrow band around it (plus a tail due to dispersion) and, quite frequently, the rest of the spectrum is swamped in noise. Raw GPR data frequently require post-acquisition processing, as they usually provide only approximate target shapes and distances (depths).

There are several methods to de-noise two dimensional data, focus on single or multiple scales and extract geometrical information. Almost all of them have been described in the excellent and comprehensive review of Jacques et al. (2011). They can be broadly classified into two categories: Directional Filters and Multi-Resolution Analysis (MRA).

Directional Filters (Directional Wavelets) are useful in many image processing tasks such as texture analysis, edge detection, image data compression, motion analysis, and image (signal) enhancement. Steerable Wavelets are an early form of Directional Filters (Freeman and Adelson, 1991; Simoncelli et al. 1992) and are closely related to the Gabor wavelets (e.g. Feichtinger and Strohmer, 1998, 2003; Lee, 2008). The Steerable Wavelets are based on directional second derivatives of a Gaussian function, while the Gabor wavelets are produced by a Gabor kernel, which is a product of an elliptical Gaussian and a complex plane wave. Tzanis (2013) discussed another class of two-dimensional directional filters, the B-Spline Wavelet (BSW) Filters; these are built by sidewise arranging a number of one-dimensional B-spline wavelets to form a matrix, tapering the transverse direction with an orthogonal window function and rotating the resulting matrix to the desired orientation. The BSW and Gabor Filters were applied to the analysis of heavily contaminated GPR data and haven been shown to

be very effective. These methods may successfully process information at arbitrarily fine scales and single orientations but do not allow for a different number of directions at each scale. In order to obtain multidirectional representation of the data at each scale, it is necessary to apply the same filter rotated to different angles under adaptive control and combine the outputs (e.g. Freeman and Adelson, 1991, for Steerable Wavelets; Grigorescu et al. 2003, for Gabor Filters; Tzanis, 2013, for Gabor and B-Spline Wavelet Filters). With reference to GPR data, the results are usually remarkable but from a computational point of view, not particularly inexpensive.

Wavelet-based processing and analysis methods have been extensively applied to images (extraction of information, compression and de-noising). Two-dimensional geophysical data is very similar to an image if each data point is taken to be a pixel; in consequence, the same wavelet-based methods have been quite extensively adapted to the processing of seismic and potential-field geophysical data but only rarely to GPR data. One such effective wavelet-based method commonly used for the treatment of geophysical data, is Multi-Resolution Analysis (MRA, e.g. Chui, 1992; Mallat, 1999). This is the design method of most of the practically relevant discrete wavelet transforms and the justification of the fast wavelet transform. MRA allows a space $L^2(\mathbb{R}^2)$, i.e. an image, to be decomposed into a sequence of nested subspaces (images) $L^2(\mathbb{R}^2) \supset \dots \supset V_n \supset \dots \supset V_0 \supset \dots \{0\}$, arranged in order of increasing detail (scale), that satisfies certain self-similarity relations in time/space and scale/frequency, as well as completeness and regularity relations. This way, the MRA provides a means to suppress events of specific scales locally but leave the rest of the data unaffected in general. The MRA has been introduced to the processing of reflection seismics fairly recently, with most of the related studies attempting to develop efficient noise suppression procedures in a time-frequency sense. Inasmuch as the GPR method is effectively equivalent to reflection seismics, GPR data can be processed with similar techniques. The pertinent literature (seismic and GPR) is not rich, but is steadily growing in numbers and applications (e.g. Deighan and Watts, 1997; Leblanc et al. 1998; Miao and Cheadle, 1998; Matos and Osorio, 2002; Nuzzo and Quarta, 2004; Jeng et al. 2009).

MRA, as applied in the literature quoted above, is not suitable for processing orientation-dependent information. In a manner analogous to the realization that Fourier methods are not suitable (or adaptable) for all signal processing problems, which has consequently led to the introduction of the wavelet transform, it has also become apparent that wavelets could successfully deal only with phenomena that are generally isotropic except for local irregularities (i.e. associated with isolated singularities at exceptional points); wavelets are less than ideal in dealing with phenomena occurring on curves or sheets (i.e. with singularities on curves), as for instance are edges in a two-dimensional image, or reflections and wavefronts in a seismic or GPR record.

This problem has been addressed by advanced MRA-like algorithms that have appeared recently and are collectively referred to as the “*X*-let Transform”. These include *ridgelets* (Candès, 1999; Candès and Donoho, 1999), *wedgelets* (Donoho, 1999), *beamlets* (Donoho and Huo, 2002), *bandlets* (Mallat and Peyré (2007)), *contourlets* (Do and Vetterli, 2005), *wave atoms* (Demanet and Ying, 2007), *surfacelets* (Lu and Do, 2007) and others. All these vary considerably in scope, properties and efficiency; details cannot be discussed herein but a comprehensive review can be found in Jacques et al. (2011). Other very effective and versatile approaches include the second generation *Curvelet Transform* (Candès and Donoho, 2003; 2003b; 2004a) and its derivatives/ extensions, the *Shearlet Transform* (e.g. Guo and Labate 2007) and the *Ripplet Transform* (e.g. Xu et al. 2010). The latter methods are specifically designed to associate scale with orientation; they yield optimally sparse representations of the data and have optimal reconstruction properties (see below). These very desirable characteristics have motivated the present investigation, which, however, will focus only on the more fundamental design: The Curvelet Transform (CT).

The CT is a multiscale and multidirectional expansion that formulates a sparse representation of the input data (a representation is sparse when it describes the data with a superposition of a small number

of components). The roots of the CT are traced to the field of Harmonic Analysis, where curvelets were introduced as expansions for asymptotic solutions of wave equations (Smith, 1998; Candès, 1999). In consequence, curvelets can be viewed as primitive and prototype waveforms – they are local in both time/space and frequency/wavenumber and correspond to a partitioning of the 2D Fourier plane by highly anisotropic elements that obey the parabolic scaling principle, that is their width is proportional to the square of their length. Owing to their anisotropic shape, curvelets are well adapted to detect wavefronts at different angles and scales because curvelets at a given scale locally correlate with aligned wavefronts of the same scale (given that wavefronts are actually edges in an otherwise smooth image).

Based on such properties of the curvelets, the CT provides an optimally sparse representation of objects with edges – specifically of objects which are smooth except for discontinuities along general curves with bounded curvature (twice differentiable or C^2 -continuous curve). If f_m is the m -order curvelet approximation to an object $f(x_1, x_2) \in L^2(\mathbb{R}^2)$, Candès and Donoho (2004a) show that if the object is singular along a smooth C^2 curve, the approximation error is $\|f - f_m\|_2^2 = O(m^{-2}[\log m]^3)$ and is optimal in the sense that there is no other representation of the same order m , that can yield a smaller asymptotic error. This is far better than the $O(m^{-1})$ error afforded by a wavelet approximation. Optimal sparsity also implies that one can recover curved objects from noisy data by curvelet shrinkage (analogous to wavelet shrinkage) and obtain a mean squared error that is far better than what was affordable with more traditional methods (Candès et al. 2006). In addition to the “static” view of optimal sparsity, curvelets may also formulate a “dynamic” optimally sparse representation of wave propagators (e.g. Candès and Demanet, 2005; Sun et al. 2010): curvelets can model the geometry of wave propagation by translating the centre of the curvelet along the wave path. As Candès et al. (2006) point out, a physical interpretation of this result is that curvelets may be viewed as the representation of local plane waves, with sufficient frequency localization to behave like waves and sufficient spatial localization to simultaneously behave like particles. The “dynamic” approach to curvelets will not be considered herein.

Another cardinal property of the CT is optimal image reconstruction in severely ill-posed problems and possesses microlocal properties, (i.e. localization properties dependent on both position and orientation), which render them particularly suitable for reconstruction problems with missing data. In general terms, depending on the acquisition geometry and noise characteristics, the curvelet expansion can be separated into a subset that can be recovered accurately, and one that cannot. The microlocal properties of the curvelets allow the former (recoverable) part to be reconstructed with accuracy similar to the accuracy that would be feasible if the data was complete and noise-free. To this effect, Candès and Donoho (2004b) show that for some statistical models which allow for C^2 objects to be recovered, there are simple algorithms based on the shrinkage of curvelet biorthogonal decompositions, which achieve optimal statistical rates of convergence, i.e. there is no other estimating procedure which can return a fundamentally better mean square error.

The main body of this paper is organized as follows: The 2nd Generation CT will first be introduced in Section 2. Inasmuch as the application of the method is still uncommon in Exploration Geophysics at large and GPR practice in particular, the introduction will be relatively rigorous; it will spare the reader from details and proofs but will elaborate on how curvelets are constructed and computed and how they operate on data with wavefronts. To this effect, a basic familiarity with the concepts of wavelet analysis will be helpful and sufficient. A brief introduction to the practical implementation of filtering via the CT will be given in Section 3. This will be followed by a rigorous presentation of several applications to data contaminated by high levels of noise, or featuring straight and curved reflections in complex propagation media, or both (Section 4). Finally, a discussion of the results and comparisons with other methods developed with the same objective will conclude the presentation.

2 The Second Generation Curvelet Transform

2.1 The Continuous Curvelet Transform (CCT)

A curvelet frame is a wave packet frame on $L^2(\mathbb{R}^2)$ based on a second dyadic decomposition which, in effect, comprises an extension of the isotropic MRA concept to include anisotropic scaling and angular dependence (directionality) while maintaining rotational invariance. In order to construct the curvelet frame, a *template* (basic) curvelet is required, which will generate it by translation, dilation and rotation. The elements of the curvelet family will provide a partition (tiling) of the two-dimensional Fourier plane.

Consider a function $f(x_1, x_2) \in L^2(\mathbb{R}^2)$ where $\mathbf{x} = [x_1 \ x_2]^T$ and may represent time, space or time and space variables. Next, consider the Fourier transform pair $f(x_1, x_2) \leftrightarrow F(\xi_1, \xi_2)$ where $\boldsymbol{\xi} = [\xi_1 \ \xi_2]^T$ may represent frequency, wavenumber of frequency and wavenumber variables. Let $r=|\boldsymbol{\xi}|$ be the radial coordinate and $\theta = \arctan(\xi_1, \xi_2)$ be the azimuthal coordinate in the $\boldsymbol{\xi}$ -plane. Finally, consider a partition of the polar coordinate plane in concentric annuli (coronae) according to $2^{j-1} \leq r \leq 2^{j+1}$, with each corona further partitioned into angular sectors according to $\angle(\theta) \leq 2^{-j/2}$, so as to generate *polar wedges* (Fig. 1a). The number of the wedges N_j increases like $\sqrt{1/\text{scale}}$ and doubles in every second ring so that the width of the wedges is proportional to the square of their length: this is the so called *parabolic scaling* (Fig. 1a).

Now consider a *radial* window $W(r)$ and an *angular* window $V(t)$, which must be smooth, nonnegative and real-valued. The support of W is $r \in (1/2, 2)$ and it must obey the *admissibility condition* $\sum_{j=-\infty}^{\infty} |W(2^{-j}r)|^2 = 1$ for $r > 0$; the support of V is $t \in (-2\pi, 2\pi]$ and the corresponding admissibility condition $\sum_{l=-\infty}^{\infty} V^2(t - 2\pi l) = 1$ for $t \in \mathbb{R}$. There is no other theoretical limitation on the nature of the windows, which means that they can be wavelets (e.g. as in Ma and Plonka, 2010).

The dilated basic curvelet in polar coordinates is

$$\Phi_{j,l=0,k=0}(r, \theta) = 2^{-3j/4} W(2^{-j}r) V\left(\frac{2^{\lfloor j/2 \rfloor} \theta}{2\pi}\right), \quad r \geq 0, \quad \theta \in [0, 2\pi), \quad j \in \mathbb{N}_0, \quad (1)$$

with $\lfloor s \rfloor$ denoting the integer part of s . Evidently, $W(2^{-j}r)$ isolates ξ -values in the corona $(2^{j-1}, 2^{j+1})$. Likewise, $V(2^{\lfloor j/2 \rfloor} \theta)$ isolates ξ -values in the angular sector $(-\pi 2^{-\lfloor j/2 \rfloor}, \pi 2^{-\lfloor j/2 \rfloor})$. For increasing j and decreasing scale $2^{-j} \in (0, 1]$, the breadth of W is growing and the width of V is shrinking, so that the wedges $\Phi_{j,0,0}(r, \theta)$ become longer (see Fig. 1a and 1c): this is the effect of parabolic scaling.

The complete curvelet family in the $\boldsymbol{\xi}$ -domain is generated from $\Phi_{j,0,0}$ by dilation, rotation and translation according to:

$$\Phi_{j,l,k}(r, \theta) = \Phi_{j,0,0} \left(\mathbf{R}_{\theta_{j,l}} \boldsymbol{\xi} \right) \cdot e^{-i \langle \mathbf{x}_k^{j,l}, \boldsymbol{\xi} \rangle}, \quad (2a)$$

or, in terms of the radial and angular windows,

$$\Phi_{j,l,k}(r, \theta) = 2^{-3j/4} W(2^{-j}r) \cdot V\left(\frac{2^{\lfloor j/2 \rfloor}}{2\pi} (\theta - \theta_{j,l})\right) \cdot e^{-i \langle \mathbf{x}_k^{j,l}, \boldsymbol{\xi} \rangle}, \quad (2b)$$

where, $\theta_{j,l} = 2\pi l \cdot 2^{-\lfloor j/2 \rfloor}$, $l = 0, 1, 2, \dots$, $0 \leq \theta_{j,l} < 2\pi$, is a sequence of equi-spaced rotation angles whose number varies proportionally to $1/\sqrt{\text{scale}}$,

$$\mathbf{R}_{\theta_{j,l}} = \begin{bmatrix} \cos \theta_{j,l} & \sin \theta_{j,l} \\ -\sin \theta_{j,l} & \cos \theta_{j,l} \end{bmatrix}, \quad \mathbf{R}_\theta^{-1} = \mathbf{R}_\theta^T = \mathbf{R}_{-\theta},$$

is the rotation by $\theta_{j,l}$ radians and

$$\mathbf{x}_k^{j,l} = \mathbf{R}_{\theta_l}^{-1} \begin{bmatrix} 2^{-j} & 0 \\ 0 & 2^{-j/2} \end{bmatrix} \begin{bmatrix} k_1 \\ k_2 \end{bmatrix}$$

are scaled positions with $k_1, k_2 \in \mathbb{Z}^2$ representing the translation parameters. As evident in eq. 2, the angular window V now isolates ξ -values in the angular sector $-\pi 2^{-\lfloor j/2 \rfloor} \leq \theta - \theta_{j,l} \leq \pi 2^{-\lfloor j/2 \rfloor}$. Moreover, the support of $\Phi_{j,l,k}$ does *not* depend on the translation parameters at all!

In the x -domain, the curvelet comprises a waveform defined by the Fourier Transform of Φ . Thus, it is:

$$\varphi_{j,l,k}(\mathbf{x}) = \varphi_{j,0,0}(\mathbf{R}_{\theta_l}(\mathbf{x} - \mathbf{x}_k^{j,l})). \quad (3)$$

Inasmuch as the support of $\Phi_{j,l,k}$ is independent of \mathbf{k} , the frequency localization of $\Phi_{j,l,0}$ is such that $\varphi_{j,l,0}(\mathbf{x})$ will decay rapidly outside a rectangle of size $2^{-j} \times 2^{-j/2}$ with its major axis perpendicular to the polar angle $\theta_{j,l}$ (e.g. Fig. 1b and 1d). Thus, the effective size of $\varphi_{j,l,k}(\mathbf{x})$ will also obey the parabolic scaling relationships: $\text{length} \approx 2^{-j/2}$, $\text{width} \approx 2^{-j} \Rightarrow \text{width} \approx \text{length}^2$. Moreover, $\Phi_{j,0,0}$ is by construction supported away from the ξ_2 axis (where $\xi_1 = 0$) but near the ξ_1 axis (where $\xi_2 = 0$). Therefore, $\varphi_{j,0,0}(\mathbf{x})$ will oscillate in the x_2 -direction and will be low-pass in the x_1 -direction. As evident from eq. 2, these oscillation properties are preserved during rotation and translation (e.g. Fig. 1d). Then, at any scale 2^{-j} , a curvelet will be enveloped by a ridge with effective length $2^{-j/2}$ and width 2^{-j} and will oscillate in a direction perpendicular to that ridge (see Fig. 1d).

A last matter to be considered is the “hole” arising in the ξ -plane around zero, since the rotations of the basic curvelets are defined only for the scales 2^{-j} . For a complete covering of the ξ -plane one must define a *low-pass* element W_{j_0} which is supported on the unit circle and is non-directional (isotropic). This (coarsest scale) element obeys

$$|W_{j_0}(r)|^2 + \sum_{j>j_0} |W(2^{-j}r)|^2 = 1, \quad (4)$$

so that coarsest scale curvelet will be

$$\Phi_{j_0}(\xi) = 2^{-j_0} W_{j_0}(2^{-j_0} |\xi|),$$

and will admit a x -domain representation of the form

$$\varphi_{j_0,k}(\mathbf{x}) = \varphi_{j_0}(\mathbf{x} - 2^{-j_0} \mathbf{k}).$$

Based on the above construction principles, a *curvelet coefficient* comprises the inner product between $f(x_1, x_2)$ and a curvelet $\varphi_{j,l,k}, j > j_0$:

$$c(j,l,k) = \langle f, \varphi_{j,l,k} \rangle = \int_{\mathbb{R}^2} f(\mathbf{x}) \overline{\varphi_{j,l,k}(\mathbf{x})} d\mathbf{x}. \quad (5)$$

The continuous curvelet transform will then be defined by the reconstruction rule

$$f(\mathbf{x}) = \sum_{j \geq j_0, l, k} c(j,l,k) \varphi_{j,l,k}(\mathbf{x}), \quad (6)$$

while the Parseval condition $\sum_{j,l,k} |c(j,l,k)|^2 = \|f\|_{L^2(\mathbb{R}^2)}^2$ will hold for all $f \in L^2(\mathbb{R}^2)$ ensuring a *tight frame* property. As a result of the parabolic scaling, the curvelet frame is an optimally sparse representation for functions with singularities along curves but otherwise smooth (Candès and Demanet, 2005).

2.2 The Discrete Curvelet Transform (DCT)

The formulation of the CCT is not particularly suitable for measured 2-D data which is usually obtained in the form of rectangular (Cartesian) arrays, because circular coronae and rotation are not easily adaptable to Cartesian geometries. In response, the inventors of the curvelet transform also developed discrete formulations which are suitable for Cartesian data arrays while being faithful to the mathematical formalism of the CCT.

In these formulations, the circular coronae are replaced by rectangular “coronae” (concentric rectangular annuli) and the rotations are replaced by shearing, so as to generate a *pseudo-polar* grid like the one shown in Fig. 2a. Thus, the Cartesian equivalent of the radial window W is $\tilde{W}_j(\xi) = \sqrt{U_{j+1}^2(\xi) - U_j^2(\xi)}$, $j \geq 0$,

where $U(\xi) = u(2^{-j}\xi_1) \cdot u(2^{-j}\xi_2)$ and u is a low-pass one-dimensional window that obeys $0 \leq u \leq 1$ and vanishes for all $\xi \notin [-2, 2]$. Under this definition and on including the isotropic window $\tilde{W}_{j_0}(\xi)$, of the coarsest scale, the Cartesian analogue of the admissibility condition (4) reads

$$\tilde{W}_{j_0}^2(\xi) + \sum_{j > j_0} \tilde{W}_j^2(\xi) = 1 \quad (7)$$

and can be shown to hold for all ξ . The angular window V is now taken to be

$$V_j(\xi) = V\left(2^{\lfloor j/2 \rfloor} \frac{\xi_2}{\xi_1}\right).$$

Following the above definitions, the basic curvelet in Cartesian coordinates is

$$\tilde{\Phi}_{j,l=0,k=0}(\xi) = 2^{-3j/4} \cdot \tilde{W}_j(\xi) \cdot V_j(\xi)$$

and is supported on a *trapezoidal* wedges bounded as $\{(\xi_1, \xi_2) : 2^j \leq \xi_1 \leq 2^{j+1}, -2^{-j/2} \leq \frac{\xi_2}{\xi_1} \leq 2^{-j/2}\}$, isolating the ξ -values included therein.

In order to map the basic Cartesian curvelet onto different orientations, instead of equispaced angles define a set of equi-spaced *slopes* $\tan \theta_l = l \cdot 2^{\lfloor -j/2 \rfloor}$, $l = -2^{\lfloor j/2 \rfloor}, \dots, 2^{\lfloor j/2 \rfloor} - 1$ and define

$$\tilde{\Phi}_{j,l,k=0}(\xi) = \tilde{\Phi}_{j,0,0}(\mathbf{S}_{\theta_l} \xi) \quad (8a)$$

where

$$\mathbf{S}_{\theta_l} = \begin{bmatrix} 1 & 0 \\ -\tan \theta_l & 1 \end{bmatrix}$$

is the *shear* matrix and where the admissibility condition is upheld. Eq. 10 can be written in terms of the windows \tilde{W} and V as

$$\tilde{\Phi}_{j,l,k=0}(\xi) = 2^{-3j/4} \cdot \tilde{W}_j(\xi) \cdot V_j(\mathbf{S}_{\theta_l} \xi) = 2^{-3j/4} \cdot \tilde{W}_j(\xi) \cdot V_j\left(2^{\lfloor j/2 \rfloor} \frac{\xi_2}{\xi_1} - l\right) \quad (8b)$$

and clearly isolates ξ -values in the wedge $\{(\xi_1, \xi_2) : 2^j \leq \xi_1 \leq 2^{j+1}, -2^{-j/2} \leq \frac{\xi_2}{\xi_1} - \tan \theta_l \leq 2^{-j/2}\}$.

Constructions such as those implied by eq. 8 are illustrated in Fig. 2b. In order to define the Cartesian analogues of the family $\Phi_{j,l,0} = \Phi_{j,0,0}(\mathbf{R}_{\theta_{j,l}} \xi)$ described in Section 2.1, it is sufficient to complete the curvelets $\tilde{\Phi}_{j,l,k=0}(\xi)$ by symmetry with respect to the origin and rotation by $\pm\pi/2$ radians. The complete the family $\tilde{\Phi}_{j,l,k=0}(\xi)$ generates the concentric partitioning whose geometry is shown in Fig. 2a.

In a final step, on introducing the translation parameters

$$\tilde{\mathbf{x}}_{\mathbf{k}}^{j,l} = \mathbf{S}_{\theta_l}^{-T} \begin{bmatrix} 2^{-j} & 0 \\ 0 & 2^{-j/2} \end{bmatrix} \begin{bmatrix} k_1 \\ k_2 \end{bmatrix} = \mathbf{S}_{\theta_l}^{-T} \mathbf{b}_{\mathbf{k}}^j,$$

and using eq. 8b, the Cartesian equivalent of eq. 2 can be written thus:

$$\tilde{\Phi}_{j,l,k}(\xi) = \tilde{\Phi}_{j,0,0}(\mathbf{S}_{\theta_j}\xi) \cdot e^{-i\langle \tilde{\mathbf{x}}_k^{j,l}, \xi \rangle}.$$

As with its CCT counterpart, the x -domain representation of the Cartesian curvelet comprises a waveform defined by the Fourier Transform of $\tilde{\Phi}$ and is:

$$\tilde{\varphi}_{j,l,k}(\mathbf{x}) = \tilde{\varphi}_{j,0,0}\left(\mathbf{S}_{\theta_j}^{-1}(\mathbf{x} - \tilde{\mathbf{x}}_k^{j,l})\right).$$

It follows that the discrete Cartesian counterpart of the curvelet coefficients is:

$$\tilde{c}(j,l,k) = \langle f, \tilde{\varphi}_{j,l,k} \rangle = \sum_{x_1, x_2} f(\mathbf{x}) \overline{\tilde{\varphi}_{j,l,k}(\mathbf{x})}. \quad (9)$$

Finally, the discrete curvelet transform will then be defined by a reconstruction formula analogous to eq. 6:

$$f(\mathbf{x}) = \sum_{j \geq j_0, l, k} \tilde{c}(j, l, k) \tilde{\varphi}_{j,l,k}(\mathbf{x}), \quad (10)$$

The implementation of eq. 9 is not straightforward; the difficulty is that on using the two-dimensional Fourier Transform to obtain $\tilde{\varphi}_{j,l,k}(\mathbf{x})$ from $\tilde{\Phi}_{j,l,k}(\xi)$, one would need to evaluate the FFT on the sheared grid $\tilde{\mathbf{x}}_k^{j,l}$, where it cannot be applied. In response, two indirect solutions have been developed by Candés et al (2005): the *unequi-spaced FFT* method and the *wrapping* method.

In the USFFT method, the translation grid is rotated so as to align with the orientation of the curvelet. To do this, at each scale/angle pair (j, l) the implementation uses a non-standard interpolation scheme to obtain sampled values of $F(\xi)$ over the support of $\tilde{\Phi}_{j,l,k}(\xi)$. The inverse transform also uses conjugate gradients iteration to invert the interpolation step. In consequence, the USFFT method has a rather higher computational cost than the wrapping algorithm.

In the wrapping method the translation grid remains untilted and the same for every orientation albeit each curvelet is assigned with its proper angle. The curvelet coefficients are taken as per eq. 9, except that $\tilde{\mathbf{x}}_k^{j,l}$ is replaced by $\mathbf{b}_k^j = (k_1 2^{-j}, k_2 2^{-j/2})$ with \mathbf{b} taking values on a rectangular grid. In this case however, it is apparent that the window $\tilde{\Phi}_{j,l,k}(\xi)$ cannot fit into a rectangle of size $2^j \times 2^{j/2}$ to which an inverse FFT could be applied. The wrapping algorithm addresses this problem by periodizing the windowed ξ -domain coefficients $\tilde{C}_{j,l}(\xi) = F(\xi) \tilde{\Phi}_{j,l,k}(\xi)$ and re-indexing $\tilde{C}_{j,l}$ by wrapping it around a rectangle centered at the origin and approximately equal to $2^j \times 2^{j/2}$. If $F(\xi)$ is unity, then $\tilde{C}_{j,l}(\xi) = \tilde{\Phi}_{j,l,k}(\xi)$ and a x -domain representation of the curvelet can be obtained by inverse FFT, otherwise the curvelet coefficients are obtained by inverse FFT of $\tilde{C}_{j,l}(\xi)$. Fig. 3a illustrates shows some examples of curvelets computed with the wrapping method at different scales, orientations and (arbitrary) translations.

Fig. 3b shows how curvelets interact with data and elongate curved objects in particular. Specifically, Fig. 3b-i illustrates a 512×512 data set featuring a wavy up-dipping set of intermittent reflections. The data was decomposed into six scales with the second coarsest scale ($j = 2$) comprising 24 angles (six per quadrant) and the number of angles doubling in every second scale. Fig. 3b-ii shows the complete set of curvelet coefficients for scales one to four as a single image, with the 5th and 6th scales comprising of almost entirely of negligible coefficients and omitted for clarity in the presentation. As evident from the hitherto discussion as well as from Fig. 4, curvelets are elongate and slender waveforms with length proportional to $2^{-j/2}$ and width proportional to 2^j ; they oscillate in their transverse direction and, in consequence, are low-pass in their longitudinal direction. Curvelets can interact with curved objects in three ways:

1. When the curvelet and the object intersect while aligned in their longitudinal directions, the transverse oscillatory part of the curvelet will locally match the same-scale component of the object and will encode this information in the corresponding set of curvelet coefficients which will have *significant* amplitudes.
2. When the curvelet and the object intersect at an arbitrary angle, the matching of the same-scale content will be imperfect with the best part of the information lost to the curvelet's low-pass longitudinal action: the curvelet coefficients will have small amplitudes.
3. When the curvelet and the object do not intersect, the coefficients will be near zero.

As evident in Fig. 3b-ii, only a handful of coefficients have noteworthy amplitudes, specifically those with indices $j=4, l = 3-6$ (top left) and their symmetric with respect to the origin (bottom right), which are significant, and those with indices $\{j = 3, l = 4-6\}$ and their symmetric, which are very weak. Fig. 3b-iii shows the curvelets $\{j = 4, l = 5\}$, $\{j = 4, l = 7\}$ and $\{j = 3, l = 5\}$, at arbitrary translations so that they could be displayed on the same image. Fig. 3b-iv illustrates a partial reconstruction of the data from the coefficients $\{j = 4, l = 5\}$ only! This curvelet has a slope of -110° and is almost perfectly aligned with the main trend of the "reflections" shown Fig. 3b-i, extracting a clear and strong component of their signal. Fig. 3b-v illustrates a partial reconstruction of the data from the coefficients $\{j = 4, l = 7\}$ only. This curvelet has a slope of -94° and is intercepting the reflections at an angle of 14° – evidently, it cannot match a signal component of any significant amplitude and the coefficients and reconstruction have insignificant amplitudes. Finally, Fig. 3b-vi illustrates a partial reconstruction of the data from the coefficients $\{j = 3, l = 5\}$ only. This curvelet is perfectly aligned with the main reflections but has the wrong scale – it extracts only a very weak background component associated with the longer ξ -components of the data. It turns out that the data can be reconstructed to within 96% from the coefficients $\{j = 3, l = 4-6\}$. This demonstrates how curvelets may assist in the retrieval of scale-and-orientation dependent information from GPR data.

3 GPR data Analysis with the Curvelet Transform.

The DCT has been implemented in the software package CurveLab, written by E. Candés, L. Demanet and L. Ying and available at <http://www.curvelet.org>. The package contains Matlab and C++ implementations of both the USFFT and Wrapping methods. In the work presented herein, only the wrapping method has been implemented for being computationally more efficient. The utility of the CT will be demonstrated via a piece of software specifically developed to facilitate the interactive application of the DCT and to visualize and control the process; a fully functional version of this application is already available in the matGPR software (e.g. Tzanis, 2010), currently located at <http://users.uoa.gr/~atzanis/matgpr/matgpr.html>.

For a given dataset, the software inquires for the number of scales, with $j = 1$ corresponding to the (coarsest-scale) inner isotropic partition. It also inquires for the number of angles at the second coarser scale ($j = 2$), i.e. the first scale at which an angular decomposition is computed (the number of angles doubles in every second scale). The DCT is then computed with the option that yields real-valued curvelet coefficients: at any given scale, if L is the number of angles, then there will be $L/2$ ‘cosine’ coefficients stored with indices $1 \dots L/2$, as well as $L/2$ ‘sine’ coefficients stored by symmetry of $L/2$ with indices $L/2+1 \dots L$. The coefficients are indexed in a clockwise sense starting at the top-left corner of the north quadrant.

The finest level scale extracts the highest frequency/ longest wavenumber content, with $j = J_e = \log_2(n/2)$ corresponding to the Nyquist, and where n is the horizontal or vertical dimension of the data matrix. The design of appropriate basis functions at the outermost dyadic corona is not straightforward due to difficulties relating to issues of over- or under-sampling at the high- ξ end of the spectrum (Candés et al. 2006). One apparent solution is to assign wavelets instead of curvelets to the finest scale and treat it with isotropic Cartesian windows $\tilde{W}_{J_e}(\xi)$ constructed so that $\tilde{W}_{J_e}^2(\xi)$, together with the curvelet windows, form a partition of unity as in eq. 7. The wavelet coefficients can, then, be obtained by inverse FFT. This approach is simple but not consistent with the idea of directional basis elements at the finest scale. Proper curvelet-based remedies for tiling the finest scale have been proposed by Candés et al. (2006). Note, however, that GPR data is usually oversampled, at least with respect to the central frequency of the Tx antenna. In consequence, there is little, if any, useful information at the high frequency scales which usually comprise random noise. In consequence, the wavelet-based remedy for the finest level scale was also adopted in this implementation of the DCT.

After the DCT is computed, the upper-right diagonal of the (pseudo-polar) tiling of the ξ -plane – or f-k plane in the case of GPR data – is displayed as shown in Fig. 4, for a hypothetical 512-by-512 data matrix decomposed into six scales and 24 angles at the second coarser scale. It is important to note that the lengths of the horizontal and vertical axes are drawn according to the horizontal and vertical dimensions of the data matrix and not according to units of wavenumber and frequency. Each trapezoidal wedge represents the support of a curvelet and is associated with the corresponding set of curvelet coefficients. More precisely, the graphical object associated with each wedge is assigned with the indices of the corresponding cosine *and* sine coefficients, while it is also set up to function as a virtual switch whose On/Off state is controlled by the screen pointing device (e.g. the mouse). All the wedges are initially displayed in their ‘On’ state, which is indicated by shading. The ‘Off’ state is indicated by a blank wedge. The coarsest level isotropic partition is displayed as a rectangle at the centre of the tile. The finest level scale is displayed separately at the space that would have been occupied by the lower-left diagonal and illustrates the associated set of wavelet coefficients. Both the coarsest and finest scale objects function as virtual switches just like the trapezoidal wedges.

It is possible to decide which coefficients to include (exclude) from a processed (reconstructed) version of the input data by pointing and clicking inside a trapezoidal wedge or rectangle. If the switch

is ‘On’, this will negate the sets of cosine and sine coefficients associated with it and will toggle its state to ‘Off’, blanking it out (Fig. 4). The negated coefficients may be restored by clicking inside a blank switch, in which case its state is reset to ‘On’ (shaded). It is also possible to toggle entire scales or angular subsets of a scale, by using appropriate GUI controls (not shown in Fig. 4). A partial or whole reconstruction of the data can be computed at any time, with GUI controls also not shown.

4 Examples

The utility and versatility of the Curvelet Transform will now be demonstrated with five applications to data from archaeometric, geotechnical and hydrogeological surveys, contaminated by high noise levels and/or featuring straight and curved reflections in complex propagation media. The first, second and fourth data sets have also been presented by Tzanis (2013), as part of the demonstration of directional and multidirectional B-Spline Wavelet and Gabor filters. In this way, comparison between effective, single-scale directional filtering methods and the multi-scale Curvelet Transform will also be possible.

The data of Fig. 5a was collected as part of an archaeometric survey with a GSSI SIR-2000 system and an antenna with a nominal central frequency of 400MHz. The raw radargram is shown as measured: it is quite noisy and comprises a $512 \text{ sample} \times 1024 \text{ traces}$ section with a sampling rate of 0.1957ns (total time window = 100ns) and trace spacing 0.01075m (section length = 11m). Two apparent and significant features in this section are the signature of a buried wall at distances 1.5 – 2.5 m and traveltimes 30 – 70 ns and an up-dipping reflector which is clearly seen between the coordinates (60ns, 6m) and (49ns, 7.8m), while there’s quite clear indication that it may extend bilaterally to later times/shorter distances (approx. 66ns/5m) and earlier times/longer distances (approx. 37ns/10m).

The radargram was decomposed into six scales with the second coarser ($j=2$) scale comprising 28 angular wedges. After some straightforward experimentation, it is easy to see that the main noise components comprise: a) Very low frequency isotropic interference ($j = 1, f < 110 \text{ MHz}, k < 1.9 \text{ m}^{-1}$); b) Low frequency, mainly horizontal ringing with frequencies $f \leq 210 \text{ MHz}$. c) High frequency bursts, localized and mainly horizontal, such that $f \geq 848 \text{ MHz}$; d) Broadband spatial variation of vertical to sub-vertical orientation. The noise can be almost precisely excised by negating all the curvelet coefficients save for those shown in Fig. 5b (left), i.e. by partially reconstructing the data based on the subset of coefficients $\{j = 3, l \in [1, 14] - [7, 8]\} \cup \{j = 4, l \in [1, 14]\}$. The image of the wall at around 2 m is now clear. Images of additional, possibly man-made structures are also apparent between the ordinates 6 m – 9 m and 25 ns – 50 ns, while the up-dipping reflector is also more clearly discerned. There is some residual ringing left, which cannot be removed without detrimental effects to the data – it is represented by the curvelets $\{j = 4, l \in [7, 8]\}$. The up-dipping reflector can be isolated by negating all the curvelet coefficients except for those in $\{j=4, l \in [4, 6]\}$, as shown in Fig. 5c. Notably, this subset comprises curvelets exactly parallel ($j = 5$) and sub-parallel to the dip of the reflector and frequencies 429 MHz – 848 MHz. The dipping reflector, not only stands out clearly and its lateral extent beyond the initially observable range is confirmed, but owing to the special microlocal features which render curvelets ideal for reconstruction problems with missing or hidden data, it is also optimally recovered and appears to be almost continuous across the section.

The second example may be familiar to several GPR practitioners: it is the radargram distributed with the GPR analysis package of Lucius and Powers (2002). The original section was measured in B-scan equal time spacing mode at the Norman (Oklahoma) Landfill with a GSSI SIR-2000 system and a 500MHz low power antenna; it was subsequently pre-processed (transformed to equal trace spacing

and resampled to 512 samples \times 512 traces, so that it now has a sampling rate of 0.1988 ns (time window equals to 101.7ns) and a trace spacing of 0.0387 m (section length is 19.8m). The section is shown in Fig. 6a and can be seen to suffer from crossing clutter, characteristic of multiple small targets or rough reflective surfaces. The noise can be locally strong, but it does not completely overshadow the data which is still interpretable. Accordingly, in this example the performance of the proposed analysis scheme can be precisely evaluated because the observer can see exactly what lies behind the noise.

In this example, the radargram was decomposed into six scales with the second coarser ($j=2$) scale comprising 24 angular wedges (the number of wedges doubles in every second scale). The clutter waveforms dip at high angles and comprise spatial rather than temporal features. They comprise two groups, one with shorter spatial widths and higher intensity, as for instance between the ordinates 2 – 4 m and traveltimes 20 – 60 ns, and one with longer spatial widths and lower intensity, as for instance between the ordinates 9 – 12 m and traveltimes 60 – 80 ns. The spatial widths of both groups can be roughly measured at several locations in the radargram; they average to approx. 0.25m, which would imply expected wavenumber(s) of the order of 4m^{-1} and would place them near the boundary of the fourth ($2.18\text{ m}^{-1} < k < 4.29\text{ m}^{-1}$ and the fifth ($4.29\text{ m}^{-1} < k < 8.63\text{ m}^{-1}$) scales. Fig. 6b illustrates a model of the clutter (right panel) reconstructed from the curvelet coefficients included in the subset $\{j = 4, l \in [13, 24]\} \cup \{j = 5, l \in [25, 48]\}$, as shown in the left panel.

A simple inspection of the data will show that the main reflections from subsurface are interfaces exhibit *apparent* dip shallower than 45° and are associated with spatial widths (scales) of metric order. Likewise, an inspection of individual trace spectra, as well as of the f-k spectrum will show that the data is disproportionately rich in low frequencies, with the peak located in the neighbourhood of 300MHz (on average). This would place the main components of the structural information in the third and fourth scales where $207\text{ MHz} < f < 835\text{ MHz}$ and $1\text{ m}^{-1} < k < 4.29\text{ m}^{-1}$. Thus, it is possible to obtain a representation of the data without clutter and low frequency/short wavenumber interference and without significant loss of structural information. This can be achieved via a partial reconstruction based on the curvelet subset $\{j = 3\} \cup \{j = 4, l \in [1, 12]\} \cup \{j = 5, l \in [1, 24]\}$; the result is shown in Fig. 6c.

The third example illustrates the capability of the curvelet transform to extract geometrical information at any scale or combination of scales. Fig. 7a illustrates a B-scan radargram collected with a Måla GPR system and 250MHz antenna in a flat open-air parking lot that was paved on above massive fragmented limestone. The data is shown after pre-processing with time-zero adjustment, global background removal, with the “inverse amplitude decay” technique (e.g. Tzanis, 2010, p25), resampling to a 512 sample \times 1024 trace matrix (the sampling rate is 0.3818 ns and trace spacing 0.0313 m) and, finally, f-k time migration with a velocity of 0.085 m/ns (the velocity was independently estimated in the field).

Noise is not a significant problem for this data set, although the migration has introduced widespread low amplitude/ low frequency/ short wavenumber spatio-temporal interference, as well as low amplitude artefacts in the bottom-left quadrant, due to moderate noise affecting the original data at that part of the section. The main structural features observed in the radargram are:

- a) Down-dipping (approx. 20°)¹ reflections which are attributed to faulting. Along the traces of these structures one may observe clusters of strong reflections corresponding to areas of intense fragmentation and small scale karstification. This process has led to the formation of larger scale features, such as is the lens-shaped feature between the ordinates 12 – 20 m and traveltimes 100 – 150 ns.

¹ The dip angle measurements were performed on a depth migrated section not shown for the sake of brevity, and were verified by field observations.

- b) Low amplitude steeply up-dipping (-55° to -45°) quasi-linear reflections due to short, small-aperture antithetic fractures. There appears to be an association between the clustering of these fractures and the clustering of reflections along the fault walls.
- c) Weak intermittent reflections, some of which are scattered in the radargram and some of which may form an obscure, broken, gently up-dipping chain between the ordinates 10 – 25 m and traveltimes 60 -20 ns. The nature of these features is not clear in the image of Fig. 7a.

Since the detection of fractures has always been a major application of GPR, this data is suitable for demonstrating the utility of the curvelet transform in a low noise environment.

Because the steeply up-dipping linear reflections exhibit rather fine spatial and temporal scales and a limited range of dip angles, the Curvelet Decomposition comprised 7 scales, 32 angles at the second coarser ($j = 2$) scale. The up-dipping reflectors have spatial widths of the order of 0.18 – 0.28 m, therefore expected wavenumbers of the order of $3.5 - 5.5 \text{ m}^{-1}$. This means that they belong to the 5th ($2.65 \text{ m}^{-1} < k < 5.33 \text{ m}^{-1}$) and 6th ($5.33 \text{ m}^{-1} < k < 10.64 \text{ m}^{-1}$) scales. Their apparent azimuth in the t-x domain can also be measured: in the un-migrated section it ranges between -80° and -70° ; in the migrated section between -70° and -60° . Accordingly, the reconstruction is based only on these two scales and only on curvelets supported on wedges sub-normal to the apparent dip of the linear reflections.

The results are shown in Fig. 7b, which illustrates a partial reconstruction based on the coefficients $\{j = 5, j = 6, l \in [55, 63]\}$ only. As scrutiny may show the reconstruction accurately represents one for one the images of the small-aperture fractures which can now be identified, mapped and analyzed much easier. Notably, the low frequency/ short wavenumber noise, as well as all every geometrical feature outside the reconstruction range has disappeared from the processed radargram. A little caution is, nevertheless, required so as not to misinterpret for structure, the components of the migration artefacts (at the bottom-left quadrant) which are conformal to the geometry of the curvelets used in the reconstruction.

Fig. 7c shows a partial reconstruction of reflections with slopes (dips) in the range -45° to 47° , i.e. without interference from steeply dipping structures and noise, long period/ short wavenumber noise and exactly horizontal residual ringing at frequencies higher than 220 MHz. This was performed using the subset of coefficients $\{j = 4, l \in [5, 14]\} \cup \{j = 5, j = 6, l \in [9, 28] - [16, 17]\}$. In addition to providing a clear view of the main down-dipping reflections from the faulting structures, this image also clarifies the existence of the gently up-dipping weak reflections discussed above. It is revealed that the suspected “obscure, broken, up-dipping chain between the ordinates 10 – 25 m and traveltimes 60 -20 ns” is there indeed; it is quasi-continuous and forms a laterally coherent structure extending to the left of that range, whose slope can now be measured and is found to be approx. equal to -15° . Similar features, albeit not of the same lateral extend, can be observed at several places in the reconstructed section and they can be seen to interact with the down-dipping reflections, as for instance around (16m, 40ns), around (12m, 100ns) and elsewhere. This is evidence that they comprise a second family of antithetic fractures.

The fourth example is similar to the third, with the difference that the geometrical information and the propagation medium are much more complex. Details about the geological setting of the survey and the can be found in Tzanis (2013) and only a brief recount will be given herein. The data was collected with a Måla GPR system and 250MHz antenna at the ridge of Mt Ktenias, Greece, as part of a geotechnical survey to investigate ground conditions at a site were high rising wind power generators were to be built. The ground comprises dipping, thin-plated limestone with intercalations of argillaceous material, intensely fragmented by faulting and multi-phase jointing. Karstification has nucleated at the loci of faults and major joints, with many cracks and karstic voids subsequently filled with lateritic material. Fig. 8a shows the example section after time-zero adjustment, global background removal, AGC with a 20ns Gaussian-tapered window, elimination of antenna self-clutter,

resampling to a 1024 sample \times 1024 trace matrix (the sampling rate is 0.3818 ns and the trace spacing 0.0313 m) and, finally, f-k migration with a velocity of 0.0975 m/ns. The velocity was estimated by direct measurement in the field and the migration introduced widespread low amplitude/ low frequency/ short wavenumber spatio-temporal interference, more evident toward the latter times of the radargram.

The existence of numerous linear or quasi-linear reflection events with variable length and dip can be easily recognized at several locations. As in the previous example, these are due to small aperture fractures. Careful inspection of the data shows that there are two kinds of quasi-linear reflections with different and measurable spatial widths that cluster around approx. 0.27 m and 0.5 m. This would imply the existence of two kinds of fractures respectively associated with expected wavenumbers of the order 4 m^{-1} and 2 m^{-1} , i.e. that the reflections are of rather fine spatial and temporal scales. Accordingly, the Curvelet Decomposition applied to this data comprised 7 scales, and 28 angles at the second coarser ($j = 2$) scale. In this scheme, both kinds of reflection belong to the 6th ($7.01 \text{ m}^{-1} > k > 3.56 \text{ m}^{-1}$) and 5th ($3.56 \text{ m}^{-1} > k > 1.77 \text{ m}^{-1}$) scales.

The most prominent of these reflections are steep and rather strong; their apparent angular distribution is limited to a relatively short arc they can be easily isolated. Fig. 8b presents a partial reconstruction based on the subset of coefficients $\{j = 5, j = 6, l \in [36, 41] \cup [44, 49]\}$. These waveforms will henceforth be referred to as “Type A”. If these features are filtered out of the data (by negating their associated curvelet coefficients), the existence of a second family of reflections can be observed (the interim result is not shown for economy in the presentation): their apparent inclination is a little above $\pm 45^\circ$, they are quite weak of amplitude and therefore obscured by more powerful data components and very difficult to observe in the original data. With a little experimentation these features can be isolated using the subset of coefficients $\{j = 5, j = 6, l \in [1, 3] \cup [26, 35] \cup [50, 56]\}$; the result is presented in Fig. 8c and they will henceforth be referred to as “Type B”.

Type B reflections dip at $\pm 20^\circ$ to $\pm 30^\circ$ rather consistently². They also clearly have shorter wavenumbers than Type A reflections and they can be adequately reconstructed with curvelets of the 5th scale only. Type A reflections are dipping at $\pm 50^\circ$ to $\pm 60^\circ$ and are generally of longer wavenumber, but they require curvelets of both the 5th and 6th scales to be faithfully reconstructed. The angular relationship between the up- and down-dipping reflections indicate that either type of reflections may comprise the signature of a conjugate system of fractures. The larger amplitudes of Type A reflections may also imply that they may have been generated by a younger phase of deformation (than Type B), with fractures gaping or filled with lateritic material as actually observed in the field).

Another way of abstracting and interpreting information will now be discussed. The visual inspection of the data clearly indicates the existence of areas rich in low frequencies. The effect should be a consequence of the properties of the material filling these areas, i.e. preferential absorption of high frequencies in high attenuation domains. An analysis of the *centroid frequency*³ (CF) reported for this data set by Tzanis (2013) indicates the existence of a complex propagation medium in which there are areas of severe high-frequency attenuation and areas of low, or altogether low attenuation, mainly observed below the 100ns line, from which there are no reflections and the CF is heavily influenced by the characteristics of random noise. High attenuation is particularly evident in a rather broad region between 12–28 m, which extends to at least 140ns between 20–25m, as well as in an up-dipping area at the far right of the section, collocated with a fault. No gradual shift of the CF was observed, implying that dispersion is not strong.

² *Ibid.* 1.

³ The Centroid Frequency is the location of the “centre of mass” of the signal spectrum; this is expected to decrease (increase) as a function of time, as the signal enters high (low) attenuation domains and is also expected to exhibit consistent gradual downshift in cases of dispersive propagation. For more details see Tzanis (2013) and references therein.

Fig. 8d illustrates a partial reconstruction based on the subset $\{j = 4, l \in [1, 28] - [21, 22]\}$, which comprises frequencies 233 MHz – 460 MHz, comparable to significantly higher than the nominal frequency of the antenna. Likewise, Fig. 8e illustrates a partial reconstruction based on the subset $\{j = 3, l \in [1, 28] - [20, 23]\}$, which comprises frequencies 113 MHz – 233 MHz that are lower to significantly lower than the nominal frequency of the antenna. In both cases, the effect of purely spatial disturbance have been eliminated.

As expected, the results are very different and correspond to reflectors with very different material properties. Thus, Fig. 8d depicts sharper reflections originating at low attenuation interfaces: these are highly localized in time and rich in high frequencies so that they can be observed at short periods (finer temporal scales). Conversely, Fig. 8e depicts broadly localized dull reflections from high attenuation interfaces that absorb high frequencies and enrich the long period content of the signal. The dull reflectors can be seen to comprise quasi-continuous anastomosing horizons, or to cluster in relatively narrow and vertically extended complexes. Given the geological situation of the study area, the former comprise interfaces between limestone fragments filled with high attenuation material, in which the larger and internally less damaged blocks appear in the form of lenses (hence the anastomoses). The latter (clusters) are signatures of cavities filled with high attenuation material. Examples of such structures can be observed between 20–30 m and 20–150 ns, which is the signature of a karstic cavity beneath a bowl-shaped sinkhole, and the up-dipping fault at the far right of the section. In all cases, the dull reflectors are collocated with the low CF domains and the filling material is lateritic in composition. As mentioned above, at travel times longer than about 100ns the attenuation is low and the radargram is void of any significant reflection. Inasmuch as the signal penetrates to the corresponding depths –dull reflections from the karstic cavity are observed to at least 150ns – these areas comprise minimally damaged or even healthy rock, in which the bedding and tectonic interfaces have small apertures, are closed and/or dry and do not respond to the wavelengths of the 250MHz antenna. The fact that the filled cavity extends well into the healthy bedrock is evidence of its tectonic origin, i.e. that it nucleated in a fault or junction of faults.

The final example will demonstrate the recovery of structural information from very noisy data measured in an adverse geological setting. The data was collected at the Kato Souli plain, near the east margin of the Marathon basin (NE Attica, Greece) and in fallow field located at the north border of the Schinias wetland (natural reserve). The ground consists of thick, generally moist Holocene alluvial sediments with a significant argillaceous component and contains a shallow (< 2m) unconfined aquifer with brackish water, as it appears to be recharged from deeper water beds that are expressly saline due to extensive sea water intrusion. The data shown herein was collected with a Måla GPR system and 250MHz antenna, as part of an experiment to evaluate the feasibility of monitoring seasonal water table variations in such a high attenuation environment. Fig. 9a shows the example section after time-zero adjustment, global background removal, time gain with the “inverse amplitude decay” method and resampling to a 256 sample \times 512 trace matrix, so that the final sampling rate is 0.4848 ns and the trace spacing 0.2756 m. The beginning of the section is located approx. 20m from a well, where the salinity could be measured (approx. 50 mgr/l in Na⁺), as well as the level of the water table, which was found to be at approx. 1.6m below ground level. The end of the section is approx. 30 m away from the waterfront of the Schinias marsh. The difference in elevation between the beginning and end of the section is approx. 1.5 m.

The data can be seen to suffer from intense, (sub)horizontal antenna self clutter and severe, long wavenumber crossing clutter characteristic of multiple small targets and/or rough reflective surfaces. There's also intense (sub)vertical spatial variation due to corresponding discontinuities in the pattern of the horizontal self-clutter, as well as the signature of a shallow buried metallic object at approx. 115 m down the scan axis. The noise is generally overwhelming and the only part of the radargram with

hints of earth structural information is a strip between 10 ns and 40 ns along the section; this is expected to contain the response of the water table.

The intensity of the self-clutter and redundant, small scale data components making up the high frequency/long wavenumber noise structure may be reduced, so as to alleviate the burden of complexity to be treated with the curvelet transform. Herein, this is done with the *Karhunen-Loeve Transform* (KLT - e.g. Fukunaga, 1990), also known as the *Eigenimage* or *Eigenvector Transform*. The KLT performs the same function as the Fourier transform but with a different set of basis functions that can be derived from the (auto)covariance matrix of the process, depend on the particular matrix (image) and enable its decomposition in as an economical way as possible, thus yielding an expansion with coefficients that are truly uncorrelated. The KLT can be realized with the singular value decomposition, which for a rank R matrix \mathbf{X} with M rows and N columns is

$$\mathbf{X} = \mathbf{U} \cdot \mathbf{S} \cdot \mathbf{V}^T = \sum_{i=1}^R s_i \mathbf{u}_i \mathbf{v}_i^T.$$

\mathbf{S} is diagonal and contains the singular values of \mathbf{X} , namely the positive square roots of the eigenvalues of the covariance matrices $\mathbf{X}\mathbf{X}^T$ and $\mathbf{X}^T\mathbf{X}$, arranged in non-increasing order; s_i is the i -th singular value of \mathbf{X} . \mathbf{U} is M -by- M orthogonal with \mathbf{u}_i being the i -th eigenvector of $\mathbf{X}\mathbf{X}^T$; \mathbf{V} is N -by- N orthogonal and \mathbf{v}_i the i -th eigenvector of $\mathbf{X}^T\mathbf{X}$, so that $\mathbf{u} \mathbf{v}^T$ is an M -by- N orthogonal matrix representing the i -th eigenimage of \mathbf{X} . In general, it is possible to reconstruct a partial representation of \mathbf{X} from only some eigenimages, i.e.

$$\tilde{\mathbf{X}} \approx \sum_{i=p}^q s_i \mathbf{u}_i \mathbf{v}_i^T, \quad 1 < p \leq q < R. \quad (11)$$

This is tantamount to band-pass filtering the matrix in the energy (size) scale $[p, q]$. Low-pass and high-pass filtering is also possible by performing the summation from $i=1$ to $i=p$ and from $i=q$ to $i=R$ respectively. The application of the KLT in the analysis of GPR data is not very common. It has been extensively discussed by Cagnoli and Ulrych (2001), while there are few examples in conference presentations (e.g. Zhao et al. 2005; Rudzki, 2008; Xie et al. 2013; a very few others).

As is apparent in Fig. 9b, the self-clutter is a large scale process – it is straightforward to verify that the eigenimages associated with the first two singular values of the data matrix are exclusively associated with it. In consequence, it is possible to derive a partial (high-pass) reconstruction of the original data set, by setting $p = 3$ and $q = 256$ in eq. 11, in which the self-clutter is partially suppressed, but *without* loss of structural information. Given also that precise levelling measurements were conducted along the section, it was possible to apply a static correction, using a velocity of 0.075 m/ns, which was obtained by direct measurement in the field. The final (partially de-noised and statically compensated section is shown in Fig. 9b, where it is apparent that the high intensity/ low frequency/ short wavenumber noise has been considerably reduced.

The Curvelet Decomposition applied to the data of Fig. 9b comprised of 6 scales and 28 angles at the second coarser scale; the short size of the vertical axis (256 samples) and relatively long sampling interval do not allow higher order decomposition. Quite apparently, the self-clutter is rather broadband and is represented by (sub)vertically oriented curvelet coefficients. The remaining part of the noise is principally of high apparent dip – broadband and expressly manifested in scale 2 (low frequency/ short wavenumber, $0.078\text{m}^{-1} < k < 0.149\text{m}^{-1}$ and $40\text{MHz} < f < 89\text{MHz}$), in scale 4 ($0.305\text{m}^{-1} < k < 0.602\text{m}^{-1}$ and $169\text{MHz} < f < 346\text{MHz}$, around the nominal central frequency of the antenna), as well as in scales 5 and 6 (high frequency/ long wavenumber). After some experimentation, the reconstruction was based on the subset $\{j = 2, l \in [1, 3] \cup [5, 7]\} \cup \{j = 3, l \in [1, 6] \cup [9, 18], \cup [25, 28]\} \cup \{j = 4, l \in [1, 6] \cup [9, 14]\}$, as shown in Fig. 9c-left. The reconstructed data is shown in Fig. 9c-right.

It is apparent that the reconstruction contains a very significant low-frequency component, inasmuch as the floor of scale 2 is located at 40.284 MHz, much lower than the nominal central frequency of the

GPR antenna. This should not be a surprise: it indicates intense high frequency attenuation due to the highly absorptive ground conditions. In addition, one may note that the data is not exactly noise-free. Residual crossing clutter is apparent, as well as residual returns from the buried metallic object, but it is so severely attenuated, so as not to interfere with the structural data. There is clear evidence of previously totally obscured, low amplitude and laterally extended reflections at traveltimes between 20 ns and 80 ns, which are attributed to the bedding of the sediments. The strip between 10 ns and 40 ns now exhibits definite evidence of a laterally extended, quasi continuous structure, which contains the response of the water table. The response is rather irregular, possibly due to a correspondingly irregular soil – water interface and also due to the residual noise. However, it is located at a constant level of approx. 1.3m below ground surface and approaches the surface towards the end of the section (i.e. towards the waterfront).

The soil – water interface may be irregular by nature (formation) and the complexity of the capillary fringe above the water table. However, note that the water table response is now the largest scale structure in the processed data set. Accordingly, it can be isolated with the aid of the KLT. The top panel of Fig. 9d shows a reconstruction of the data of Fig. 9c by using only the first two eigenimages. This is an almost optimally recovered response of the water table, which as mentioned previously is observed at a constant level and is consistent with the control points at the beginning (well) and end of the section (waterfront). A reconstruction based on remaining ($p=3$ to $q=256$) eigenimages yields the bottom panel of Fig. 9d. In this higher order reconstruction, the envelope of the water table response can be seen to comprise a fuzzy domain indicating dispersive propagation.

5 Discussion and Conclusions.

The present work discusses a data processing method based on the Curvelet Transform (CT) and designed to facilitate the cancelation of complex noise and the retrieval of scale-and orientation dependent information from two-dimensional (B-scan) GPR data. The CT is a pyramidal multiscale and multidirectional decomposition (partition) of the f-k spectrum into highly anisotropic/ highly localized elements, expressed as an expansion that formulates an *optimally* sparse representation of the input data with *optimal* reconstruction property. This means that any recoverable piece of information with a given scale and orientation can be retrieved from a noisy data set (image), as if it was noise-free. By tuning the sampling rate, the order of the pyramidal decomposition (scale) and the order of the angular decomposition, one may resolve data components of at any scale and orientation, at least as fine as the order at which over- or under-sampling issues begin to hamper the computations (i.e. the limit of available information is exceeded).

The method is simple to use and very powerful: with a little trial and error the analyst may recover information about any resolvable data trait and operate with, sometimes, surgical precision. It was shown that the CT can be used to:

- a) Enhance the S/N ratio by isolating and cancelling directional noise wavefronts of any scale and angle of emergence in such an adaptive way and precision, as not to interfere with any part of the recoverable data components.
- b) Isolate/ enhance and retrieve waveforms of specific scale and geometry for further scrutiny, as for instance distinguish signals from small and large aperture fractures and faults, different phases of fracturing and faulting, bedding etc.
- c) Exploit the temporal localization characteristics of the filter outputs to investigate the characteristics of signal propagation (hence material properties), albeit indirectly. This is possible because signal attenuation and temporal localization are closely associated. Thus, interfaces in low attenuation domains will tend to produce reflections richer in high frequencies and fine-scale localization, while interfaces in high attenuation domains will tend to produce dull reflections, rich in low frequencies and broad localization.

The merits of the CT are immediately apparent, but a valid and important question is of whether other methods exist, that can offer analogous or even improved efficiency. The answer is not simple and also not negative, as will be discussed below.

The CT is, in effect, a very elaborate f-k filtering technique. In some cases with simple data and/or noise structures, conventional f-k filters may perform equally well. However, when the structural and/or noise complexity increases, conventional f-k filtering techniques may be very impractical. The advanced orientation-sensitive X-let transforms may also offer efficient alternatives, depending of course, on their design. Some older designs are certainly not as efficient; ridgelets, for instance, were intended to represent objects with discontinuities on straight lines. Other X-lets optimized for the processing of edges, (e.g. shearlets, ripples and contourlets), most of them genetically related to the CT, have similar approximation rates and may perform analogously well. When the data is strongly oscillatory, designs optimized to process oscillating textures (e.g. wave atoms) may be superior because “curvelets only capture the coherence of the pattern along the oscillations, not across” (Demanet and Ying, 2007). Adaptive low-dimensional approximations (e.g. wedgelets) and adaptive orthogonal expansions (e.g. bandlets) may perform very efficient approximations of objects with geometric singularities; however, it is doubtful whether such objects are common in GPR data. The list is certainly long and cannot be exhausted herein, to anyone’s satisfaction. Some of the advanced X-lets, specifically of the type optimized to process oscillatory patterns, will be examined in a follow-up research.

Another simple and intuitive filtering scheme proposed for de-noising and retrieving scale-and-orientation dependent information from GPR data is the directional and multidirectional B-Spline Wavelet (BSW) and Gabor filters approach (Tzanis, 2013). The data of the first, second and fourth examples presented in Section 4 above have also been treated this author and will be a basis for comparisons.

Note that there is no objective measure, for instance in the form of some metric, to quantitatively compare the CT on one hand and the BSW and Gabor filters on the other, because they are very different in their design and mode of operation: the CT is based on a precisely specified decomposition and expansion, while the BSW and Gabor filters differ between them as they are based on different wavelets (with different localization properties) and different aspect ratios. To device systematic empirical measures of the relative performance of the CT and the host of BSW and Gabor filters is not simple and beyond the scope of the present analysis, if not pointless from a practical point of view. In consequence, any comparison made herein will be qualitative and intuitive rather than analytical and rigorous. Accordingly the “comparability” in the performance of the two classes of filter should be understood in terms of similitude in their outputs with respect to the same input data set: the results are deemed “comparable” when they resolve the same temporal and spatial features with approximately matching temporal, spatial and amplitude structures and where the degree of similitude is a matter of common sense.

In the case of simple linear or quasi-linear reflectors, such as the one shown in the first example of Section 4, the output of the directional filters (Tzanis, 2013, Fig. 7) compares well with the corresponding output of the CT (Fig. 5 of the present analysis). The outputs of those particular directional filters still have some residual ringing noise due the particular choice of their aspect ratios. This can be remedied by decreasing the aspect ratio, which amounts to increasing the anisotropy of their spectral lobes in the radial direction and reduces the leakage of noise into the output data. When the anisotropy of the aligned directional filters becomes comparable to, or higher than the anisotropy of the aligned curvelets, their output can be shown to become absolutely comparable or even better than that of the CT (in a qualitative sense of course).

Caution is needed when comparing the outputs of the CT and multidirectional filters when operating on complex data. The CT employs a redundant pyramidal decomposition, usually comprising a small number of scaling steps (coronae) arranged in powers of 2. The order of the decomposition may be increased, but this may only improve resolution in the low frequency/ short wavenumber bands and cannot be increased significantly, as it is limited by the sampling rate. Thus, localization in *both* frequency and wavenumber is somewhat limited by the geometry of the decomposition, while frequency localization cannot be separated from wavenumber localization at the analyst’s discretion. The multidirectional wavelet filtering scheme proposed by Tzanis (2013) is applied by combining the outputs of the same filter rotated to different angles under adaptive control, so that it remains *tuned* at a given frequency or wavenumber. The scale depends on the order of the wavelet and the localization on the type of the wavelet and the aspect ratio (anisotropy), so that it can vary from broad to very fine, even at the same scale. This means that the multidirectional filters can be focused on very specific frequency or spatial aspects of the data, a trait that may not always be possible with a pyramidal decomposition.

If wavelets with intermediate localization properties are used, (e.g. linear or quadratic B-Splines as in the examples presented by Tzanis, 2013), the results are generally comparable for data of moderate complexity. This can be easily verified by studying Fig. 10 of Tzanis (2013) against Fig. 6b and 6c of the present analysis. The possibility to fine tune the directional filters, however, as well as the versatility of choosing the extent of frequency or spatial localization may be advantageous when attempting to resolve complex geometric information in very complex data. This can be appreciated by comparing Fig. 13a and 13b of Tzanis (2013) against Fig. 8b of the present analysis (fourth

example). In the former case it is possible to resolve Type A and B reflections by tuning multidirectional filters with intermediate localization characteristics to 4 m^{-1} and 2 m^{-1} respectively. In the latter case, the separation is not as successful, because the “central” wavenumber of Type A reflections (4 m^{-1}) is located near the boundary of the fifth and sixth scales (3.56 m^{-1}), so that information is filtered away when the fifth or sixth scales are treated separately, while localization is reduced when they are taken together. Conversely, the CT has superior angular resolution: it makes easy to completely distinguish Type A and Type B reflections by resolving small differences in their angular distribution. Moreover, the elaborate f-k filtering scheme afforded by the CT enables the successful processing of data swamped in noise as complex, as that of the fifth example above (Fig. 9a). It should not take anyone long to verify that this type of data could not have been treated effectively with directional or multidirectional filters because they have very simple spectral structures!

In conclusion, the CT offers a provably effective and powerful method to process and analyze noisy and complex data, with some limitations arising when the data is strongly oscillatory, or if very specific traits (in frequency or wavenumber) need to be resolved. These limitations can be addressed with other methods, as for instance with multidirectional filtering techniques as detailed above. In the end, the CT and multidirectional filters both provide a powerful and complementary set of tools with which to retrieve almost any recoverable structural trait in GPR data.

REFERENCES

- Candès, E., 1999. Harmonic analysis of neural networks. *Appl. Comput. Harmon. Anal.*, 6, 197-218.
- Candès, E. and Donoho, D., 1999. Ridgelets: A key to higher-dimensional intermittency? *R. Soc. Lond. Philos. Trans. Ser. A Math. Phys. Eng. Sci.*, 357, 2495-2509.
- Candès, E. and Donoho, D., 2003a. Continuous curvelet transform: I. Resolution of the wavefront set. *Appl. Comput. Harmon. Anal.*, 19, 162-197.
- Candès, E. and Donoho, D., 2003b. Continuous curvelet transform: II. Discretization and frames. *Appl. Comput. Harmon. Anal.*, 19, 198-222.
- Candès, E. and Donoho, D., 2004a. New tight frames of curvelets and optimal representations of objects with piecewise C^2 singularities. *Comm. Pure Appl. Math.*, 57, 219-266.
- Candès, E. and Donoho, D., 2004b. Curvelets: new tools for limited angle tomography, Technical Report, California Institute of Technology.
- Candès, E. J., and Demanet L., 2005. The curvelet representation of wave propagators is optimally sparse, *Comm. Pure Appl. Math.*, 58 (11), 1472–1528.
- Candès, E. J., L. Demanet, D. L. Donoho, and L. Ying, 2006. Fast discrete curvelet transforms (FDCT). *Multiscale Modeling and Simulation*, 5, 861–899.
- Cagnoli, B. and Ulrych, T.J., 2001. Singular value decomposition and wavy reflections in ground-penetrating radar images of base surge deposits, *Journal of Applied Geophysics*, 48, 175 – 182.
- Chui, C.K., 1992. An introduction to wavelets, Academic Press, New York.
- Deighan, A. J., and Watts, D. R., 1997. Ground-roll suppression using the wavelet transform. *Geophysics*, 62, 1896–1903.

- Demanet, L. and Ying, L., 2007. Wave Atoms and Sparsity of Oscillatory Patterns. *Appl. Comput. Harmon. Anal.*, 23 (3), 368-387.
- Do, M. and Vetterli, M., 2005. The contourlet transform: an efficient directional multiresolution image representation. *IEEE Trans. Image Process.*, 14 (12), 2091-2106.
- Donoho, D. and Huo, X., 2002. Beamlets and multiscale image analysis, in: T. Barth et al. (Eds.), *Multiscale and Multiresolution Methods*, Springer Lecture Notes in Comput. Sci. Eng., vol. 20, pp. 149-196.
- Donoho, D., 1999. Wedgelets: nearly minimax estimation of edges. *Ann. Statistics*, 27 (3), 859-897.
- Feichtinger, H.G. and Strohmer, T., 1998. *Gabor Analysis and Algorithms*, Birkhäuser; ISBN 0817639594
- Freeman, W. and Adelson, E., 1991. The design and use of steerable filters. *IEEE Trans. Pattern Analysis and Machine Intelligence*, 13 (9), 891-906.
- Fukunaga, K., 1990. *Introduction to Statistical Pattern Recognition*, 2nd Ed., Academic Press, London.
- Grigorescu, C., Petkov, N. and Westenberg, M.A., 2003. Contour detection based on nonclassical receptive field inhibition. *IEEE Trans. Image Process.*, 12 (7), 729-739.
- Guo, K. and Labate, D., 2007. Optimally sparse multidimensional representation using shearlets, *SIAM J. Math. Anal.*, 39, 298-318.
- Jacques, L., Duval, L., Chaux, C. and Peyré, G., 2011. A panorama on multiscale geometric representations, intertwining spatial, directional and frequency selectivity, *Signal Processing*, 91, 2699-2730; doi:10.1016/j.sigpro.2011.04.025
- Jeng, Yih, Lin, C-H., Li, Y-W., Chen, C-S. and Huang, H-H., 2009. Application of multiresolution analysis in removing ground-penetrating radar noise. *Frontiers+Innovation – 2009 CSPG-CSEG-CWLS Convention*, 416-419.
- Lee, T., 2008. Image representation using 2D Gabor wavelets. *IEEE Trans. Pattern Anal.*, 18 (10), 1-13.
- Leblanc, G. E., Morris, W. A., and Robinson, B., 1998. Wavelet analysis approach to de-noising of magnetic data. *SEG Expanded Abstract*, 554-557.
- Lu, Y. and Do, M., 2007. Multidimensional directional filter banks and surfacelets. *IEEE Trans. Image Process.*, 16 (4), 918-931.
- Lucius, J.E. and Powers, M.H., 2002. GPR Data Processing Computer Software for the PC. USGS Open-File Report 02-166.
- Ma, J. and Plonka, G., 2010. The Curvelet Transform, *IEEE Signal Processing Magazine*, 118, doi: 10.1109/MSP.2009.935453
- Mallat, S. and Peyré, G., 2007. A review of bandlet methods for geometrical image representation, *Numer. Algorithms*, 44 (3), 205-234.
- Mallat, S.G., 1999. *A Wavelet Tour of Signal Processing*, Academic Press.
- Matos, M. D. and Osorio, P. M., 2002. Wavelet transform filtering in the 1D and 2D for ground roll suppression. *SEG Expanded Abstract*, 2245-2248.
- Miao, X., and Cheadle, S. P., 1998, Noise attenuation with wavelet transforms. *SEG Expanded Abstract*, 1072-1075.
- Nuzzo, L., and Quarta, T., 2004. Improvement in GPR coherent noise attenuation using $\tau - p$ and wavelet transforms. *Geophysics* 69, 789-802.
- Rudzki, M., 2008, Coherent Noise Attenuation in the GPR Data via the Karhunen-Loéve Transform, *Proceedings*, 14th European meeting of the EAGE, Krakow, Poland, 29-30 September 2008.

- Simoncelli, E., Freeman, W., Adelson, E. and Heeger, D., 1992. Shiftable multiscale transforms. *IEEE Trans. Inform. Theory*, 38 (2), 587-607.
- Smith, H. F., 1998. A Hardy space for Fourier integral operators, *J. Geom. Analysis*, 7, 629 – 653.
- Sun, B., Ma, J., Chauris, H. and Yang, H., 2010. Solving the Wave Equation Using Curvelets, *Proceedings, 72nd EAGE Conference & Exhibition, Barcelona, Spain June 14 - 17, 2010*
- Tzanis, A., 2010. matGPR Release 2: A freeware MATLAB® package for the analysis & interpretation of common and single offset GPR data, *FastTimes*, 15 (1), 17 – 43.
- Tzanis, A., 2013. Detection and extraction of orientation-and-scale-dependent information from two-dimensional GPR data with tuneable directional wavelet filters. *Journal of Applied Geophysics*, 89, 48-67. DOI: 10.1016/j.jappgeo.2012.11.007
- Xie, X., Zeng, C. and Wang, Z., 2013, GPR signal enhancement using band-pass and K–L filtering: a case study for the evaluation of grout in a shielded tunnel, *J. Geophys. Eng.* 10 034003.
- Xu, J., Yang, L. and Wu, D., 2010. Ripplet: a new transform for image processing, *J. Vis. Commun. Image Repr.*, 21 (7), 627–639
- Zhao, A., Jiang, Y. and Wang, W., 2005. Signal-to-noise ratio enhancement in multichannel GPR data via the Karhunen-Loeve Transform, *Proccedings, Progress in Electromagnetic Research 2005, Hangzhou, China, August 22-26 2005*.

FIGURE CAPTIONS

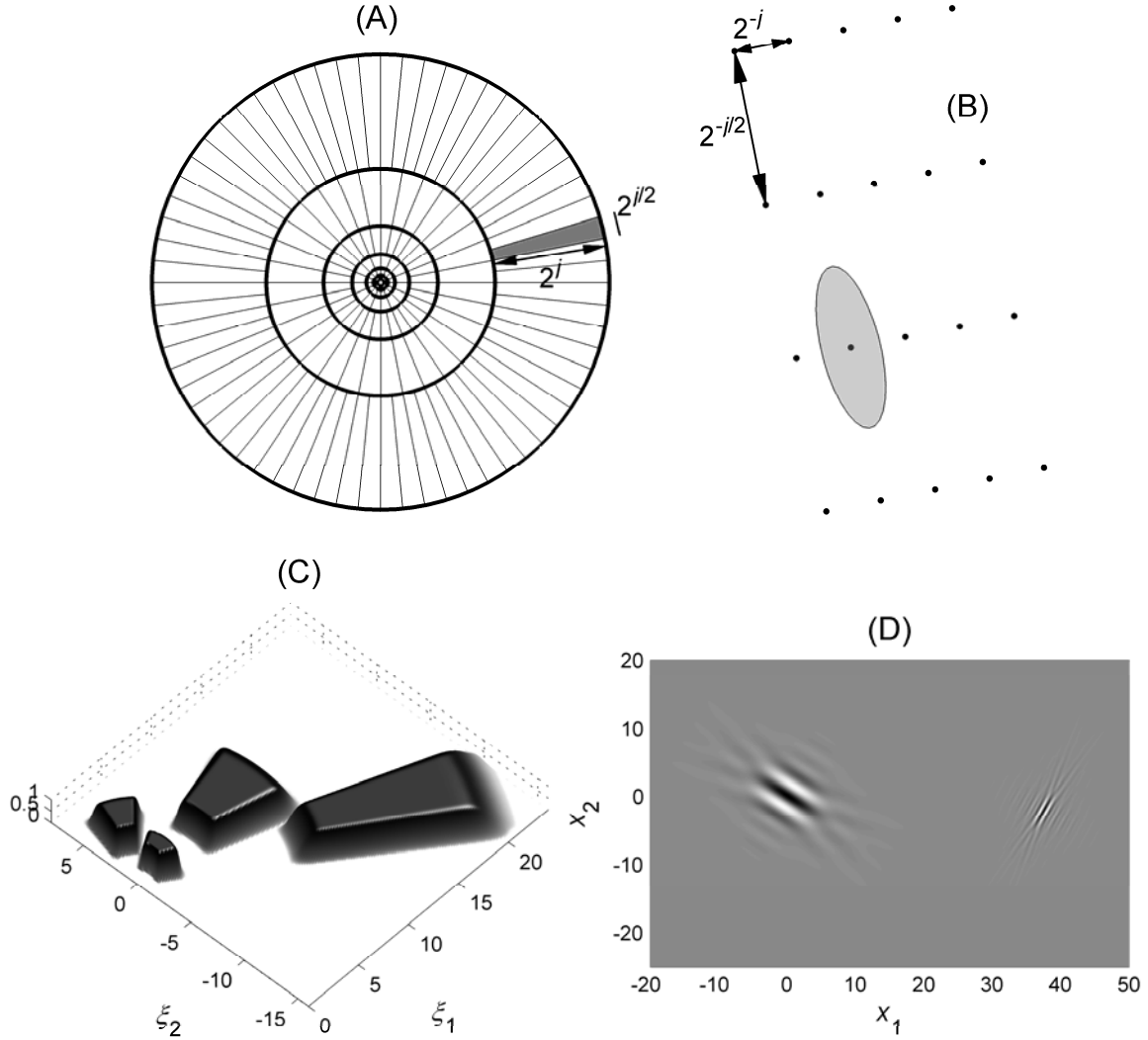


Figure 1. (a) Tiling of the ξ -plane in polar coordinates with parabolic scaling. The shaded area represents a wedge supporting a curvelet. (b) Schematic representation of a Cartesian grid in the x -domain, associated with a ξ -domain wedge like the shaded one shown in Fig. 1a. Due to the duality between the two domains, the spacing and scaling of the x -domain curvelet (represented by the ellipse) is also parabolic. (c) Some ξ -domain curvelets in perspective view: from left to right they are $\{j=1, l=0\}$, $\{j=2, l=2\}$, $\{j=3, l=0\}$ and $\{j=4, l=22\}$. (d) The x -domain curvelets $\{j=2, l=2\}$ (left) and an arbitrarily translated version of $\{j=4, l=22\}$ (right).

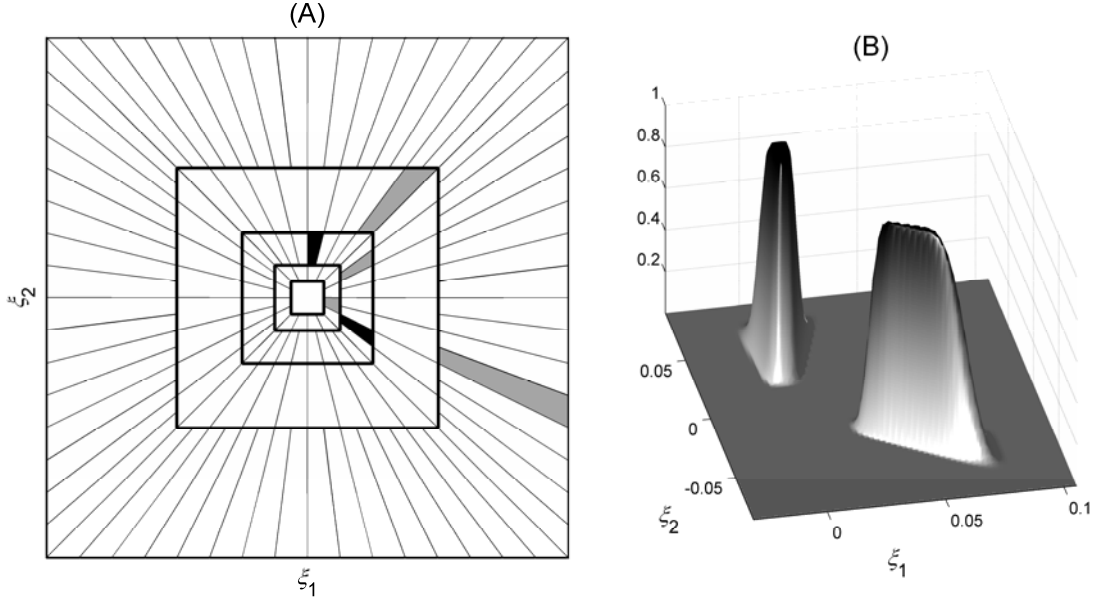


Figure 2. (A) illustrates a pseudo-polar partitioning (tiling) of the ξ -plane in Cartesian coordinates. The inner (coarsest-scale) isotropic partition corresponds to $j = 1$. The indexing of the wedges (l) counts clockwise from the top-left corner of each scale. The solid black elements at $j=3$, $l=5$ and $j=3$, $l=15$ indicates the right-hand side trapezoidal wedge that supports the curvelets shown in (B). The gray elements indicate the wedges supporting the curvelets shown in Fig. 3.

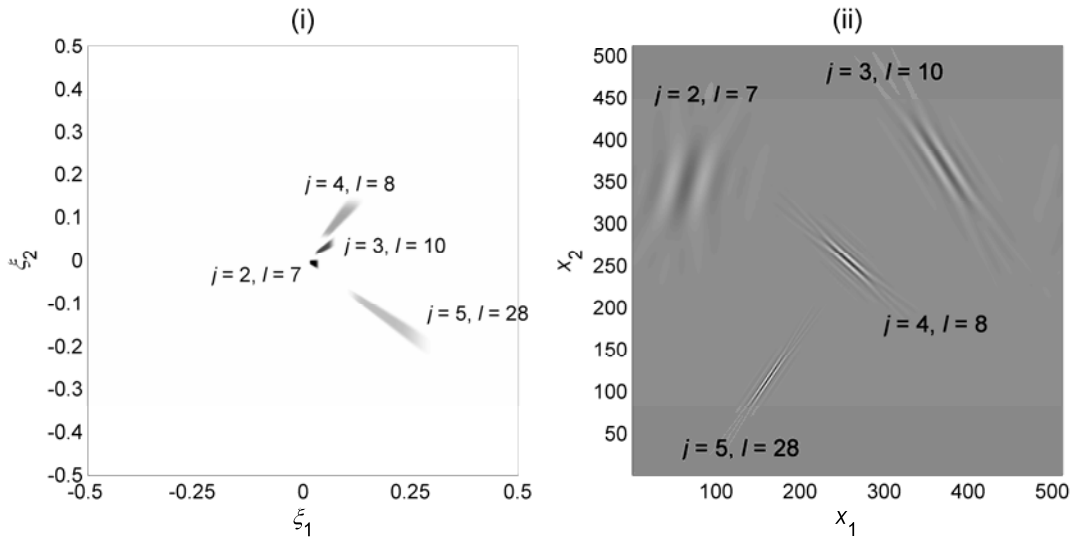


Figure 3a. (i) Amplitudes of complex ξ -domain curvelets at different scales and orientations. The trapezoidal wedges supporting these curvelets are shown in Fig. 2a. The indexing (l) increases clockwise from the top-left corner of each scale. (ii) Arbitrarily translated x -domain curvelets, corresponding to the ξ -domain curvelets of the left pane (i).

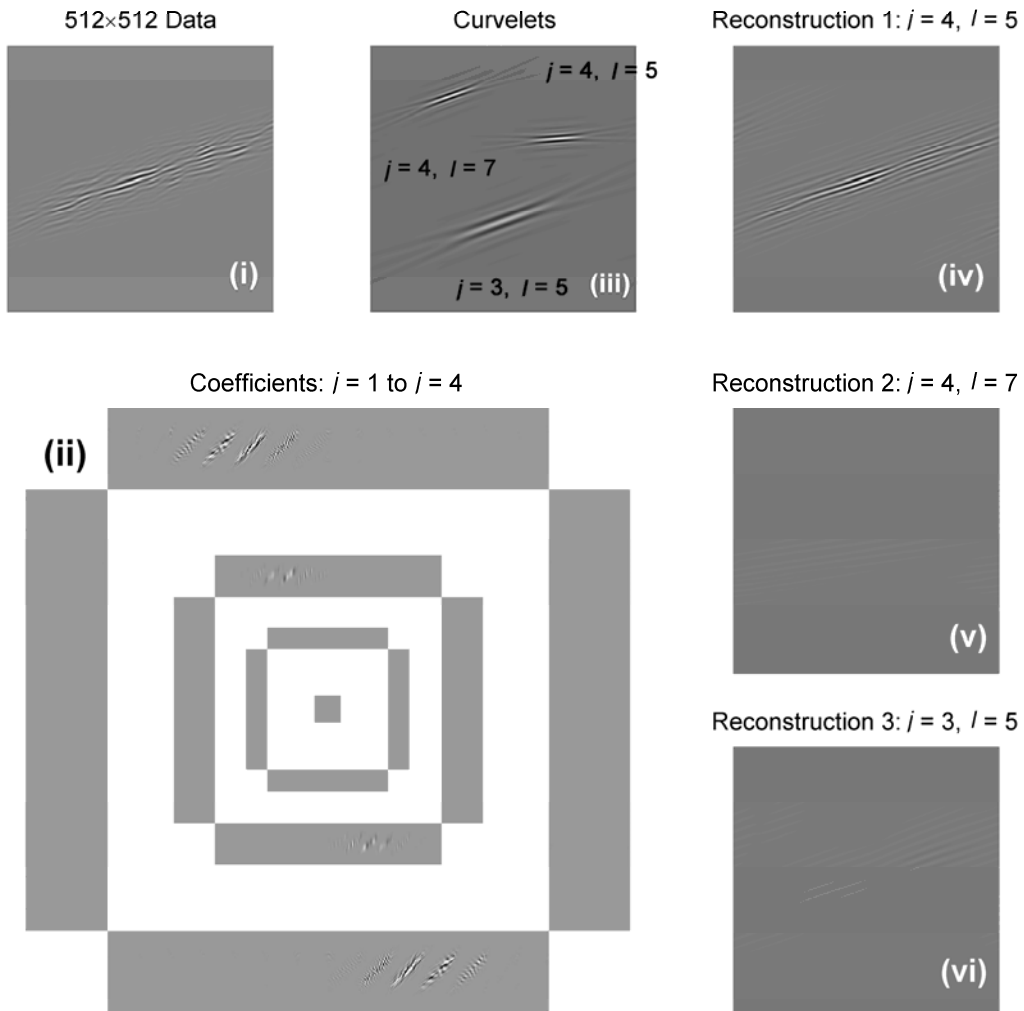


Figure 3b. A demonstration of data and curvelet interactions: **(i)** The data comprise a 512×512 matrix featuring only a set of wavy intermittent up-dipping reflections. **(ii)** The complete set of curvelet coefficients after decomposition into six scales; only the coefficients of scales one to four are shown. **(iii)** The curvelets used for the reconstructions shown in panels (iv) to (vi). **(iv)** Partial reconstruction of the data based on the curvelet $\{j = 4, l = 5\}$. **(v)** As in (iv) but for the curvelet $\{j = 4, l = 7\}$. **(vi)** As in (iv) and (v) but for the curvelet $\{j = 3, l = 5\}$.

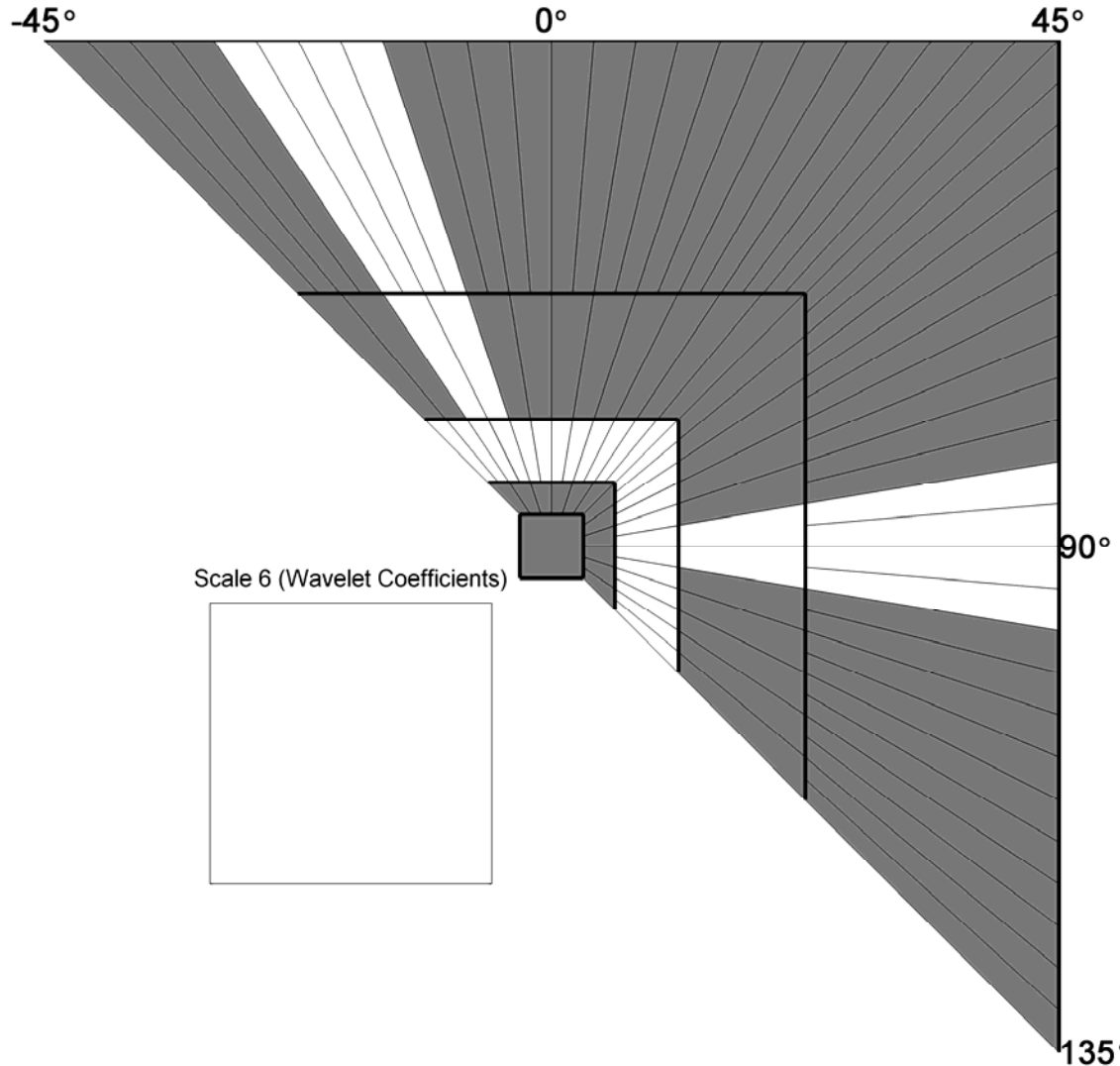


Figure 4. The upper-right diagonal (north and east quadrants) of the pseudo-polar tiling of the ξ -plane for a 512-by-512 data matrix decomposed into six scales and 24 angles at the second coarser scale ($j=2$). Each trapezoidal wedge, as well as the rectangles corresponding to $j=1$ (central) and $j=6$ (lower left), is associated with a corresponding set of sine and cosine coefficients and functions as a “graphical switch” whose state can be toggled by pointing and clicking. The “On” state is indicated with shading and the corresponding coefficients are included in a reconstruction of the input data. The “Off” state is blank and the corresponding coefficients are excluded from a reconstruction.

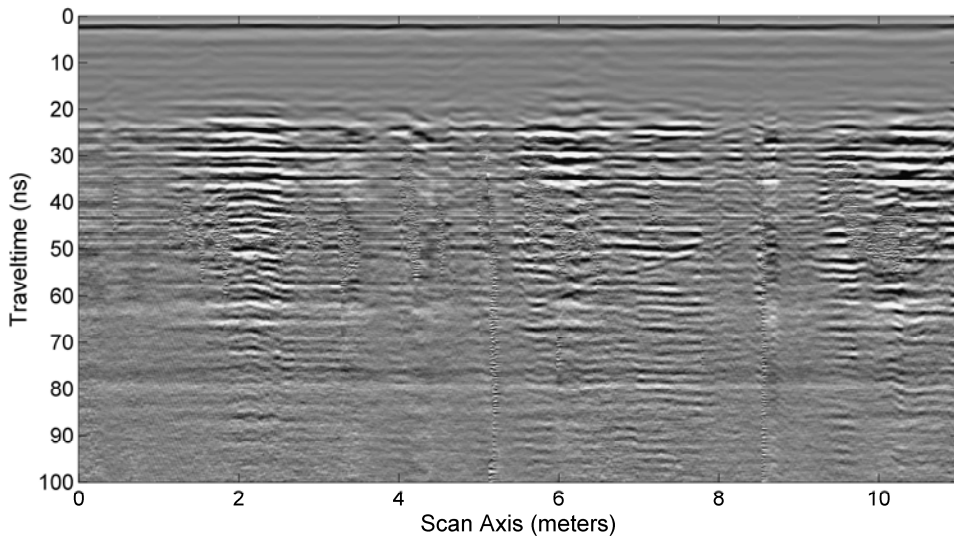


Figure 5a. B-scan radargram featuring the signature of a buried wall between the ordinates 1.5 – 2.5 m and traveltimes 30–70 ns, as well as a linear up-dipping reflector between the ordinates 49 – 60 ns and abscissae 6 – 7.8 m. The linear reflector is deeply buried in noise.

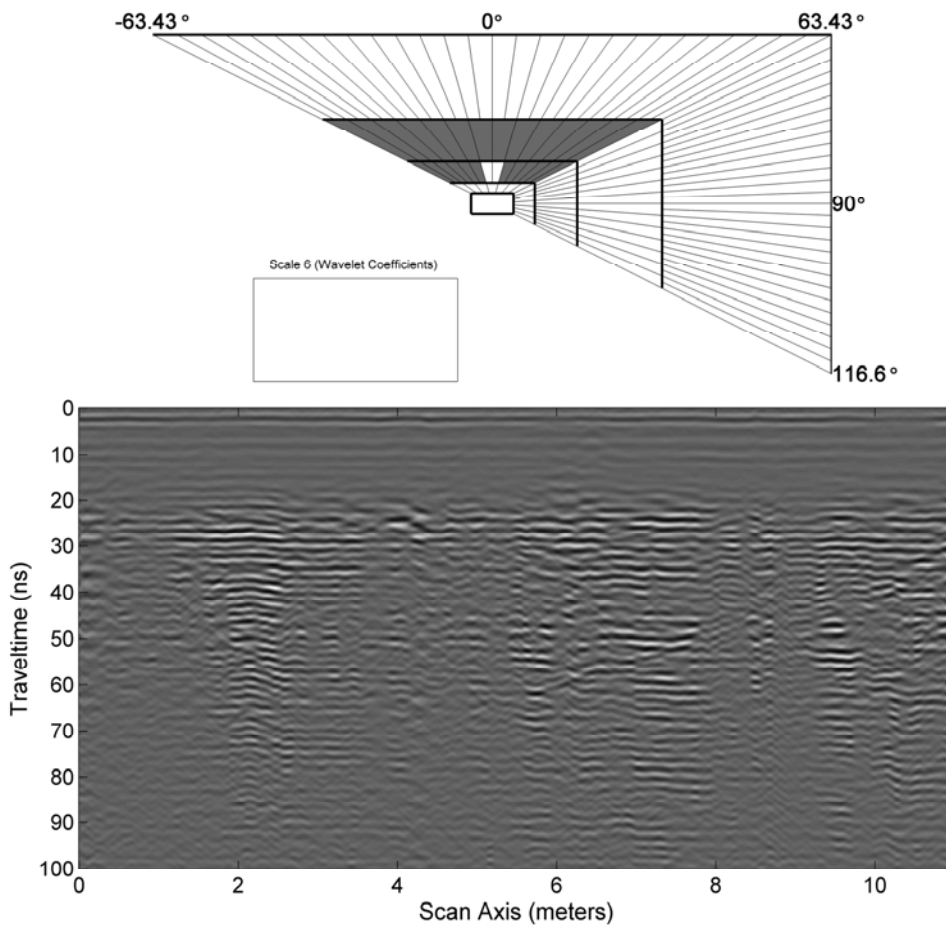


Figure 5b. The bottom panel illustrates the de-noised radargram of Fig. 5a, after negating “noise” coefficients shown in the top panel.

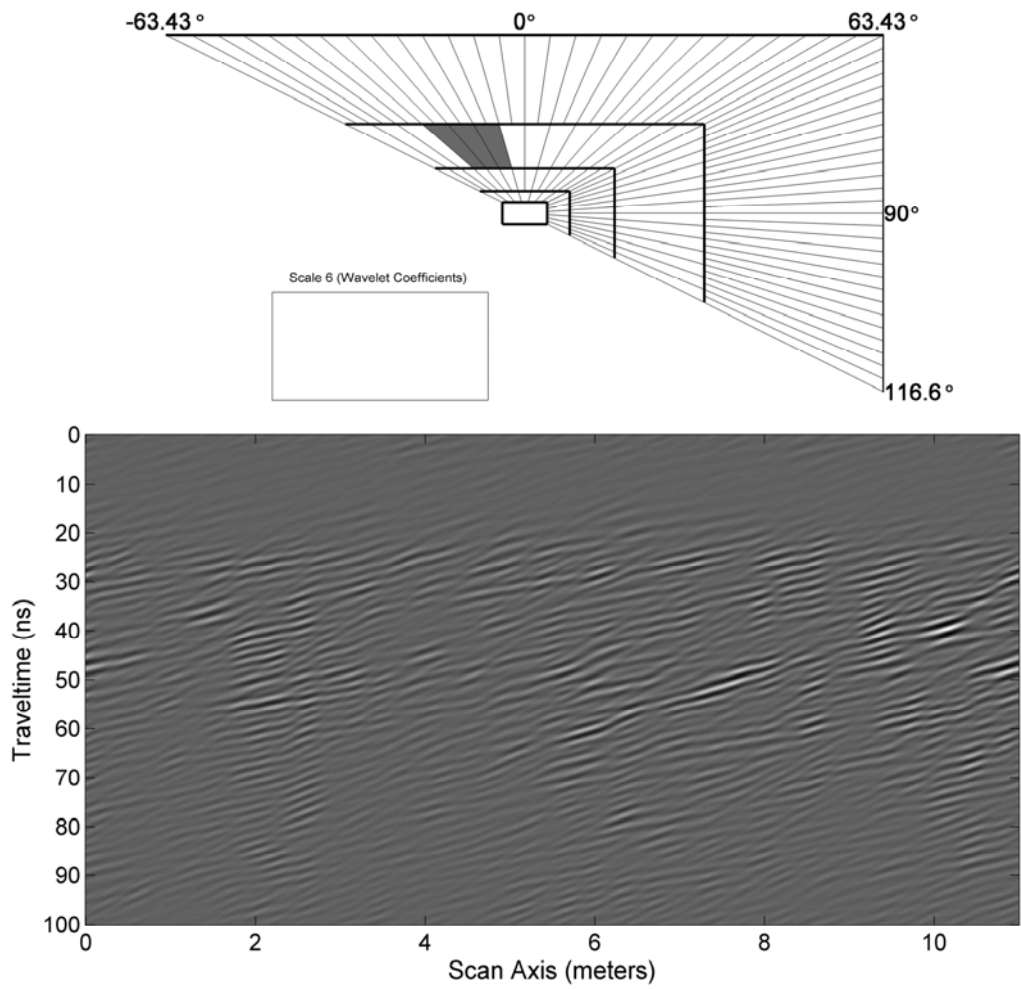


Figure 5c. The bottom panel illustrates the up-dipping reflector featured in Fig. 5a and Fig5b, reconstructed from the curvelet coefficients $\{j=4, l \in [4, 6]\}$ shown in the top panel.

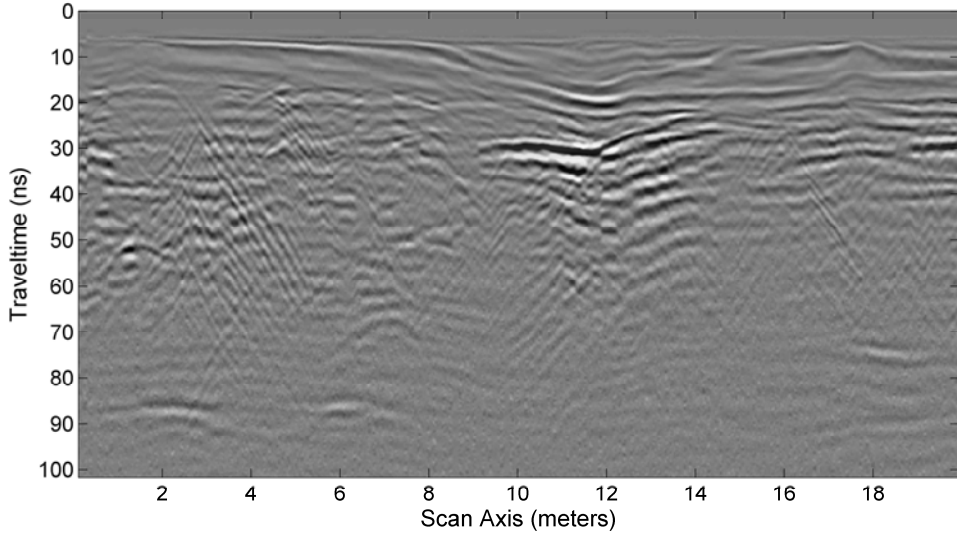


Figure 6a. The radargram distributed with the GPR analysis package of Lucius and Powers (2002), transformed to equal trace spacing and resampled to a 512×512 matrix. The data suffer from crossing clutter, characteristic of multiple small targets or rough reflective surfaces.

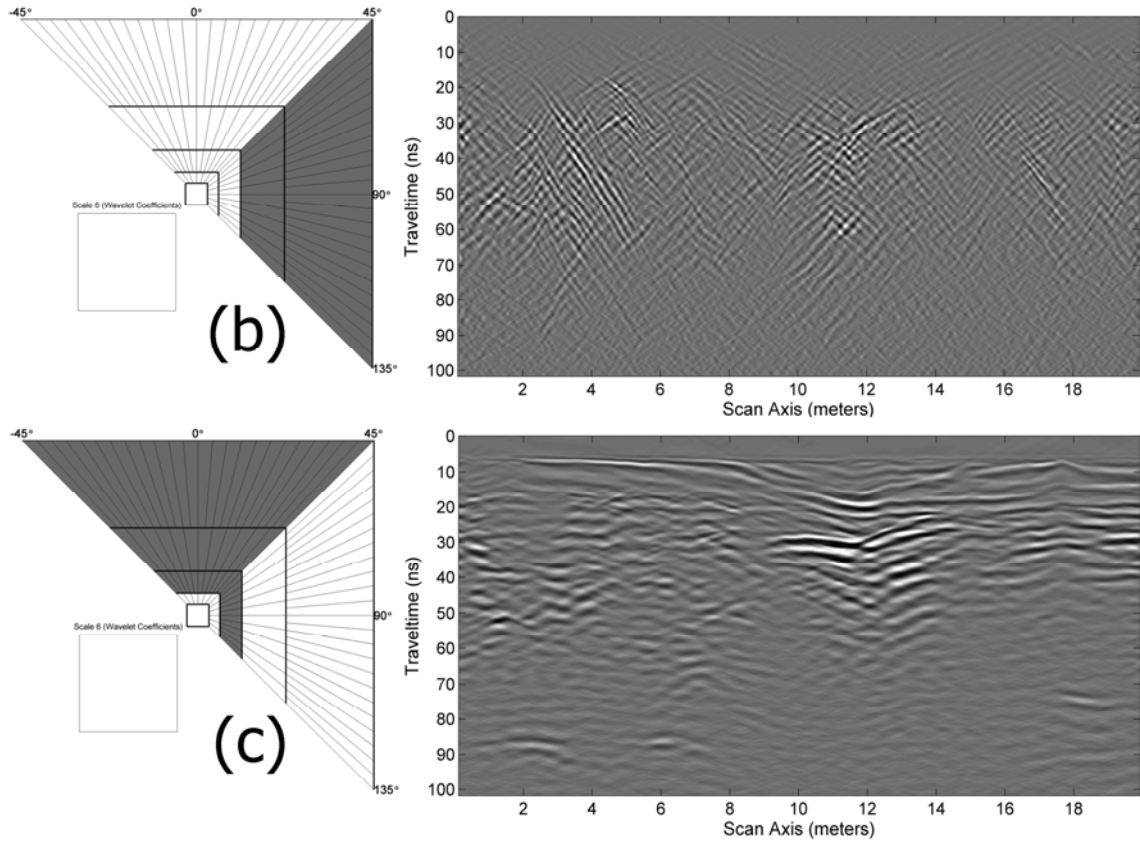


Figure 6. **(b)** The top-right panel illustrates a partial reconstruction of the data of Fig. 6a based on curvelets in the subset $\{j = 4, l \in [13, 24]\} \cup \{j = 5, l \in [25, 48]\}$ shown in the top-left panel. This effectively isolates the crossing noise process. **(c)** The bottom-right panel illustrates a clutter-free partial reconstruction of the data of Fig. 6a based on curvelets in the subset $\{j = 3\} \cup \{j = 4, l \in [1, 12]\} \cup \{j = 5, l \in [1, 24]\}$, as shown in the bottom-left panel.

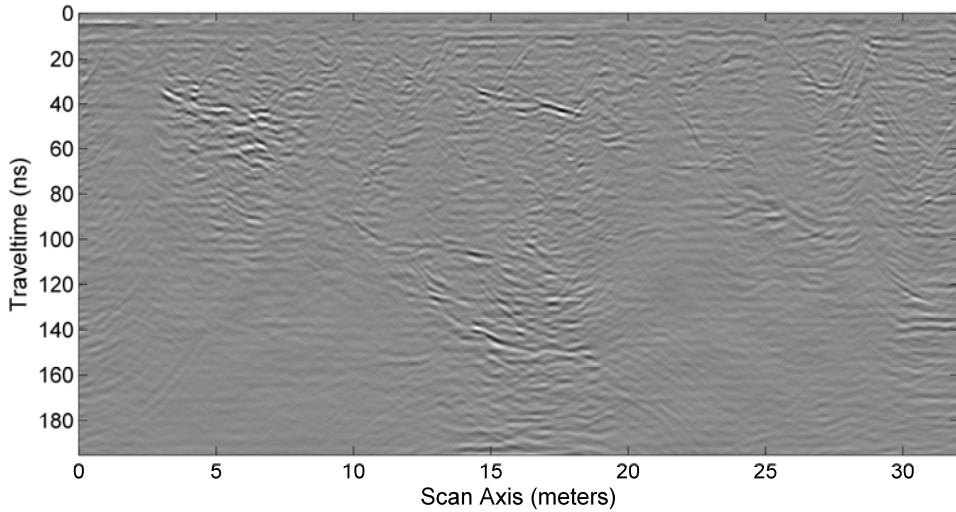


Figure 7a. A B-scan radargram obtained above massive fragmented limestone. The data has been pre-processed as detailed in the text.

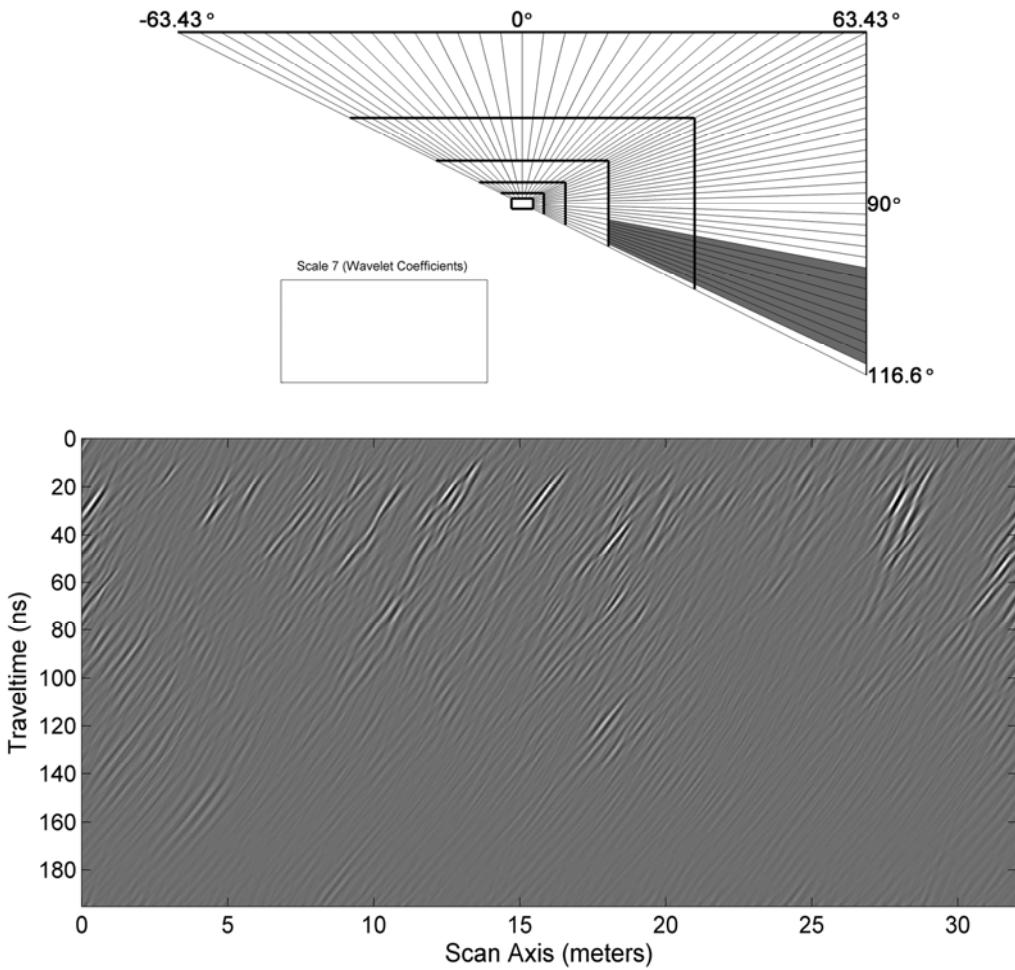


Figure 7b. The bottom panel illustrates a partial reconstruction of the migrated radargram shown in Fig. 7a, based on the subset of coefficients $\{j = 5, j = 6, l \in [55, 63]\}$ shown in the top panel. The reconstruction effectively isolates steeply up-dipping linear reflections from small aperture fractures and joints.

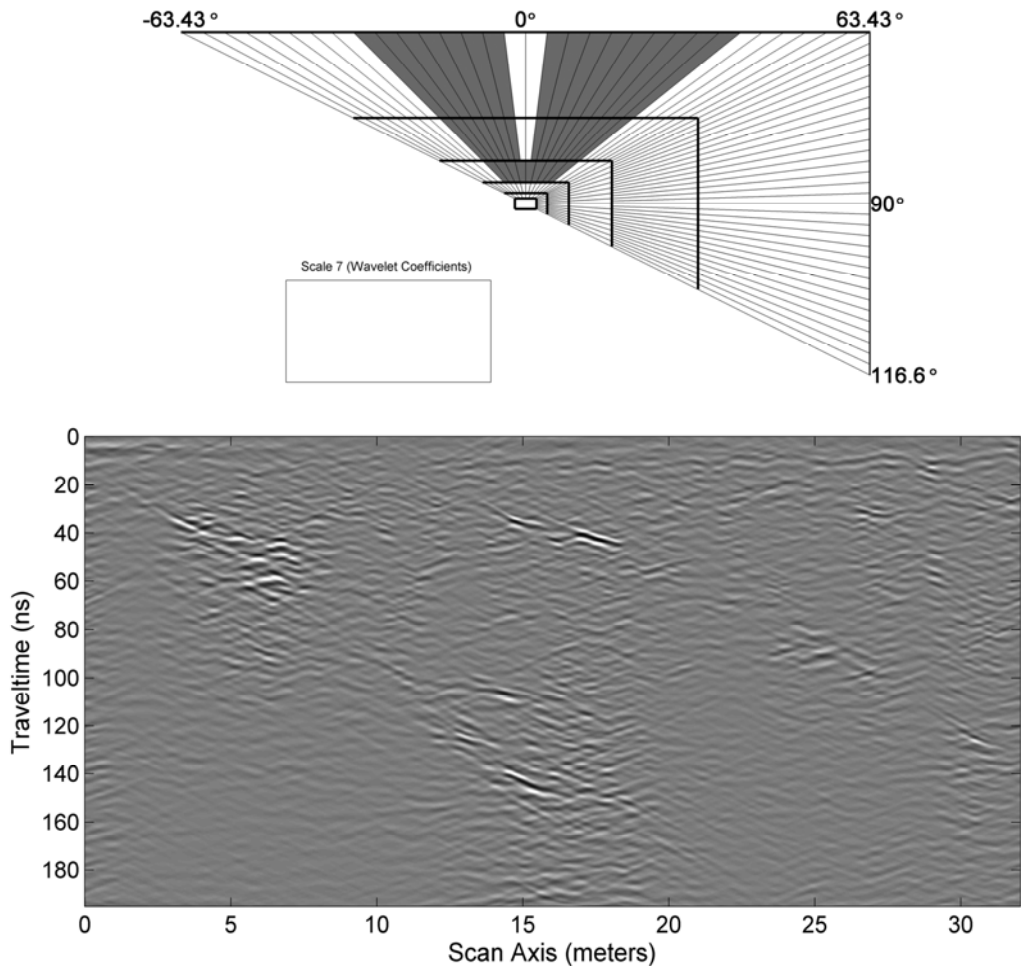


Figure 7c. The bottom panel illustrates a partial reconstruction of the migrated radargram of Fig. 7a, based on the subset $\{j = 4, l \in [5, 14]\} \cup \{j = 5, l \in [9, 28] - [16, 17]\}$ shown in the top panel.

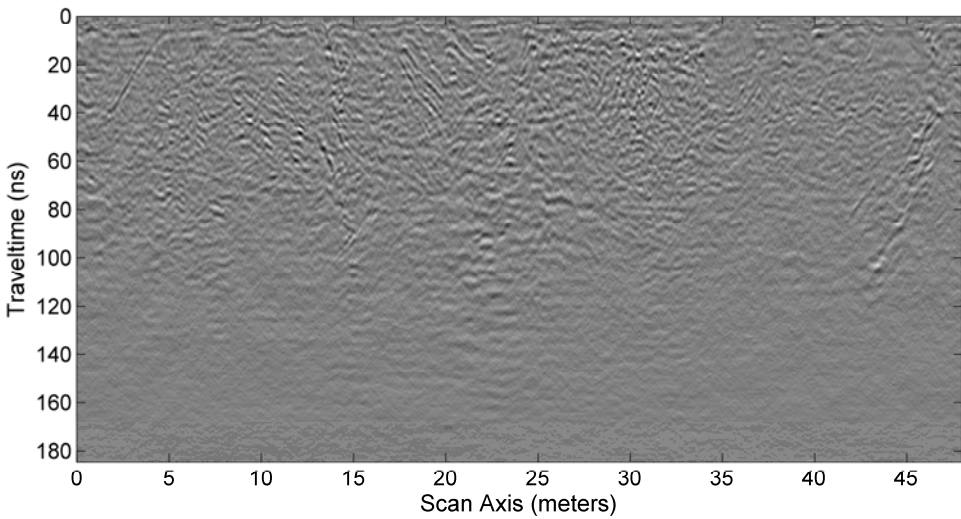


Figure 8a. Example radargram obtained at the ridge of Mt. Ktenias, Greece. The data has been pre-processed as detailed in the text and is courtesy of Mr P. Sotiropoulos, Terra-Marine Ltd (<http://terramarine.gr>).

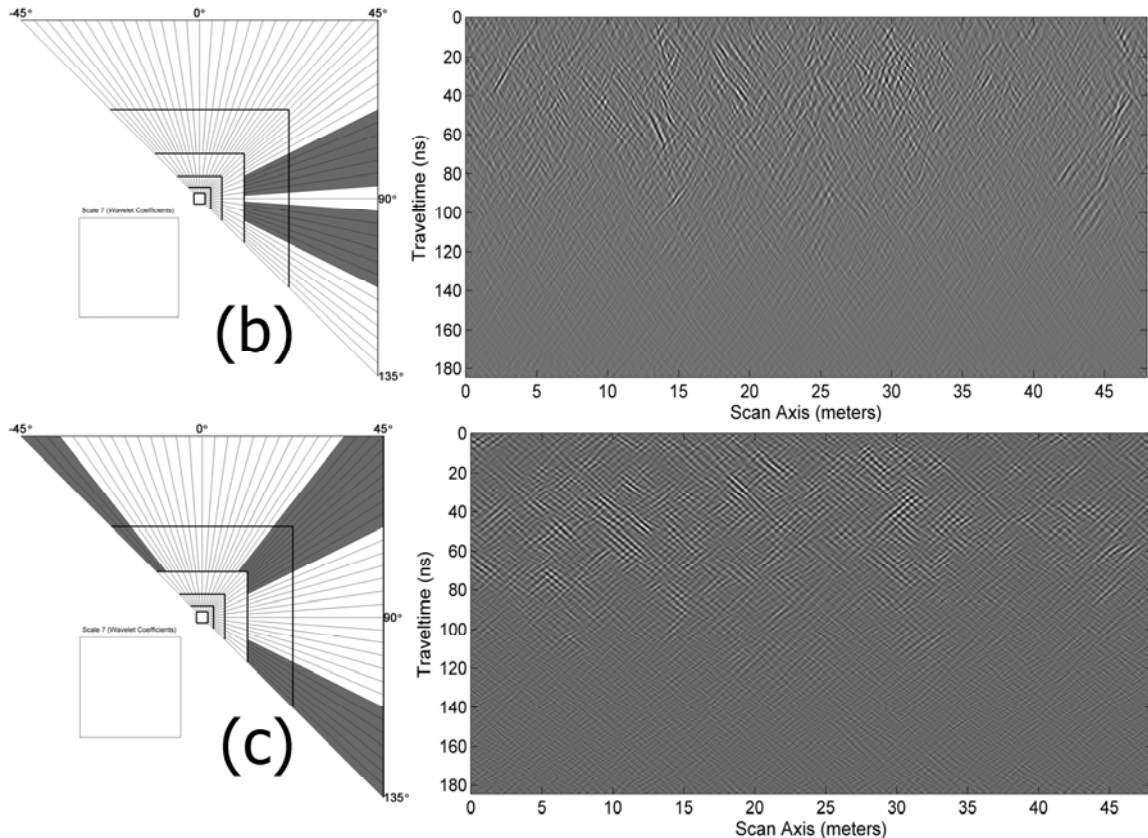


Figure 8. **(b)** The top-right panel illustrates a partial reconstruction of the GPR section shown of Fig. 8a, based on the subset of coefficients $\{j = 5, j = 6, l \in [36, 41] \cup [44, 49]\}$ illustrated in the top-left panel. **(c)** The bottom-right panel illustrates a partial reconstruction of the same data based on the subset $\{j = 5, j = 6, l \in [1, 3] \cup [26, 35] \cup [50, 56]\}$ shown in the bottom-left.

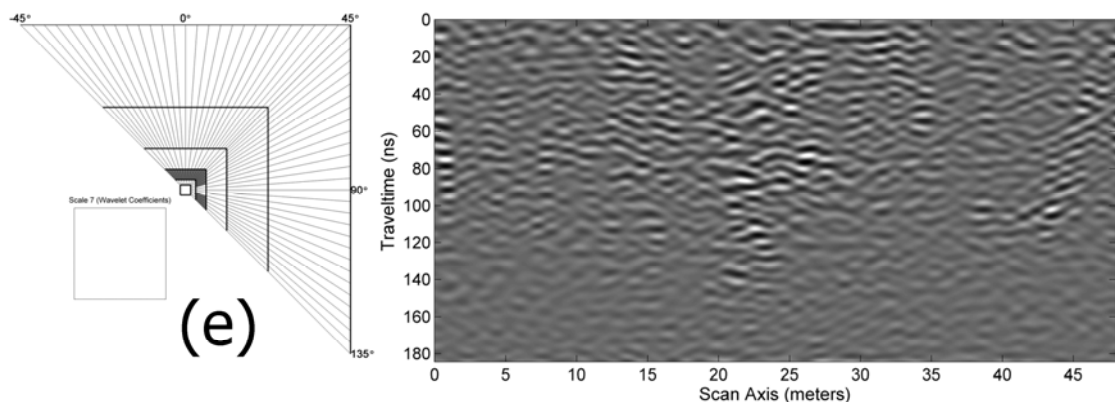
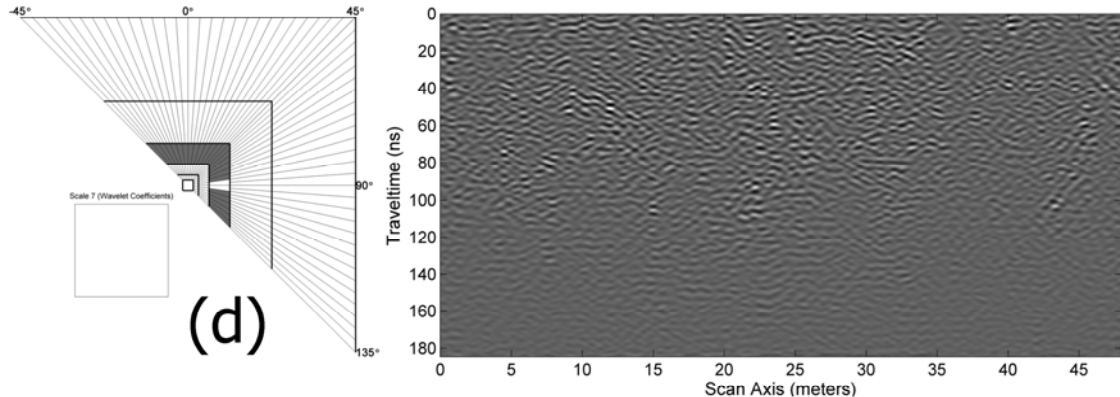


Figure 8. (d) The top-right panel illustrates a partial reconstruction of the radargram shown of Fig. 8a based on the subset of coefficients $\{j=4, l \in [1, 28] - [21, 22]\}$ shown in the top-left panel. (e) The bottom-right panel illustrates a partial reconstruction of the same radargram based on the subset $\{j = 3, l \in [1, 28] - [20, 23]\}$ shown in the bottom-left panel.

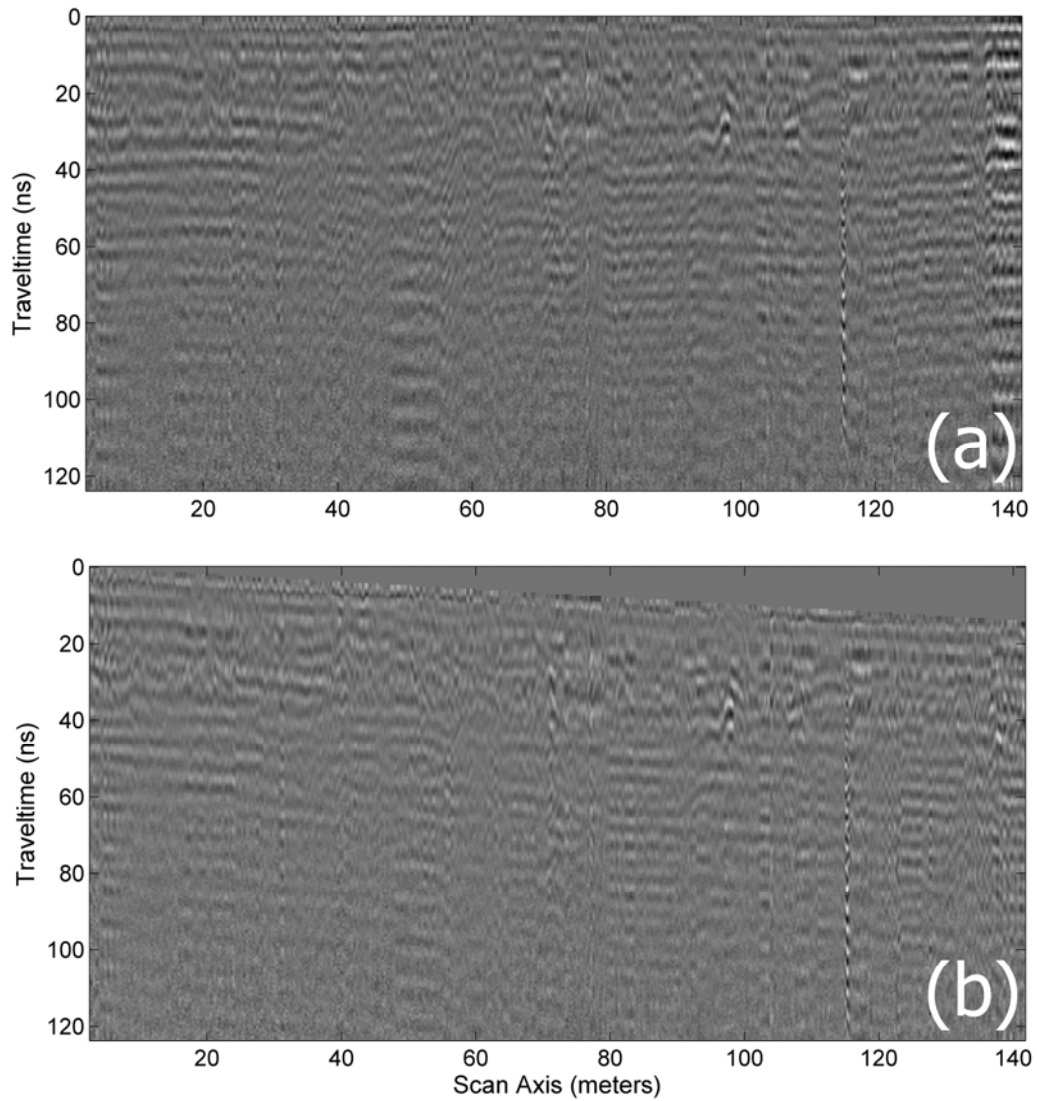


Figure 9. (a) Radargram obtained at the margin of the Schinias marsh, NE Attica, Greece. The data has been pre-processed with time-zero adjustment, global background removal and time-dependent amplification (time gain). **(b)** The data of Fig. 9a after high-pass Karhunen-Loeve filtering (eigenimages $p=3$ to $q=256$) and static correction with a velocity of 0.075 m/ns.

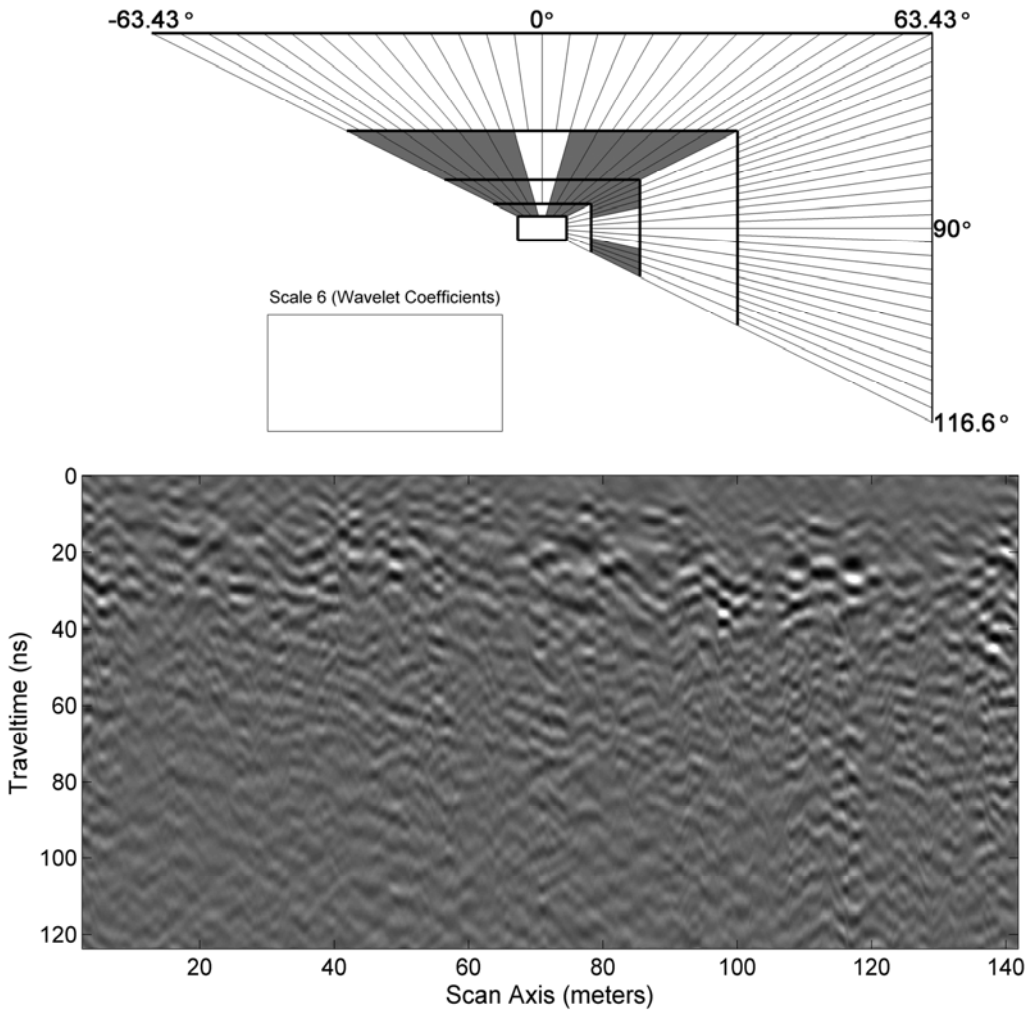


Figure 9c. The bottom panel illustrates a partial reconstruction of the section shown of Fig. 9b, based on the subset of curvelet coefficients $\{j = 2, l \in [1, 3] \cup [5, 7]\} \cup \{j = 3, l \in [1, 6] \cup [9, 18], \cup [25, 28]\} \cup \{j = 4, l \in [1, 6] \cup [9, 14]\}$ shown in the top.

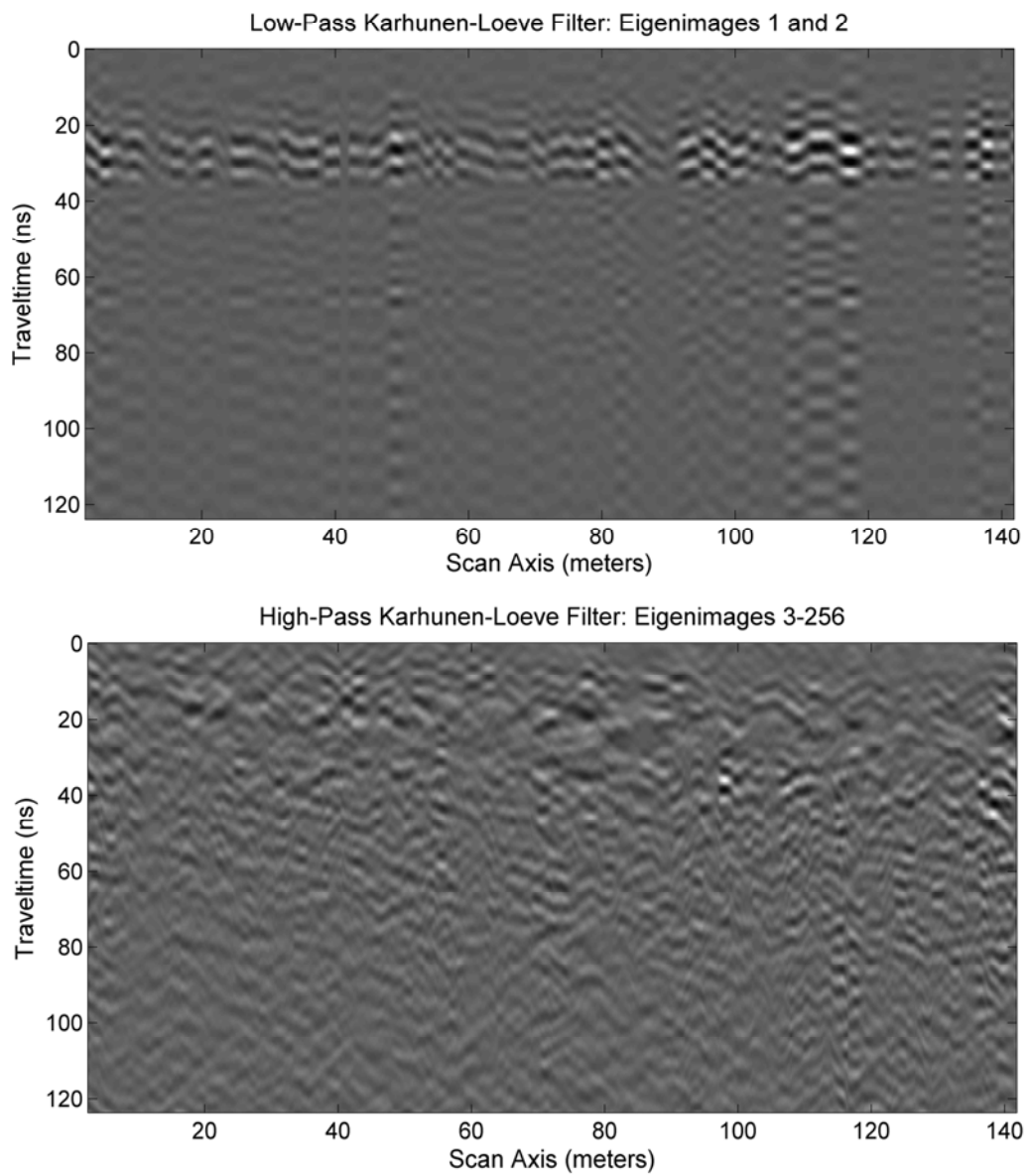


Figure 9d. Top: The data of Fig. 9c after low-pass Karhunen-Loeve filtering (eigenimages 1 and 2). **Bottom:** The same data after high-pass Karhunen-Loeve filtering (eigenimages 3-256).